

Title	水素貯蔵材料における分子吸着相互作用の第一原理解析
Author(s)	GENKI, IMAM PRAYOGO
Citation	
Issue Date	2022-09
Type	Thesis or Dissertation
Text version	ETD
URL	<a href="http://hdl.handle.net/10119/18133">http://hdl.handle.net/10119/18133</a>
Rights	
Description	Supervisor:前園 涼, 先端科学技術研究科, 博士

***Ab initio* Investigation of Molecular Adsorption in  
Hydrogen Storage Materials**

Genki Imam Prayogo

Japan Advanced Institute of Science and Technology

Doctoral Dissertation

*Ab initio* Investigation of Molecular Adsorption in  
Hydrogen Storage Materials

Genki Imam Prayogo

Supervisor: Ryo Maezono

Graduate School of Advanced Science and Technology  
Japan Advanced Institute of Science and Technology

Information Science

September 2022

# Abstract

Hydrogen is an interesting candidate for an environmentally-friendly energy carrier, due to its low weight, ability to be produced from water through electrolysis, and carbon-less combustion by-product. Storing hydrogen however, is known to be notoriously difficult, requiring very high pressure or ultra low temperature to satisfy certain industrial requirements. This remains one of the most important bottleneck to its more widespread adoption.

In a separate development, nanotechnologies have enabled high performance materials beyond what is conventionally possible. Relevant to the problem is the development of nanostructures allowing increased surface area and optimized shape, with examples such as carbon nanotubes (CNTs) and silicon carbide nanotubes (SiCNTs). To further enhance their performance, surface modifications by doping or defect formation is being continuously investigated, although the sheer amount of possible combination of materials and structures means experimental researches have seen limited progress.

Material informatics is a promising emerging field, offering faster iteration at lowered cost. With the help of massive computational facilities and multiscale modelling, from fundamental *ab initio* physics to coarse grained models with observable physical quantities, material properties can be estimated without the need for expensive experimentation. Unfortunately, the hydrogen interaction with the nanostructures is dominated by van der Waals (vdW) force, which has its origin in quantum fluctuation thus causing the popular density functional theory (DFT) to fail. Ideas for incorporating vdW into DFT have been explored in recent years, however these corrections can fail in different manner for different materials, making it difficult to judge their accuracy. If reference experimental data are widely available, it becomes a simple problem of finding which one best matches the reference, however this severely limits the reach of material informatics in handling novel materials.

Quantum Monte Carlo (QMC), in particular the diffusion Monte Carlo (DMC) is a separate approach that completely avoids the problem by solving the true many body wavefunction, therefore treating vdW by default without any corrections. In the past, its application is limited to small systems due to the lack of computational power, but with the development of supercomputers it is increasingly applied to larger problems. Moreover, the algorithm is fundamentally more amenable to parallelization than the conventional DFT, allowing it to run at a higher scale. Its accuracy means that it can be used for generating reference values in lieu of experimentation, accelerating the search for hydrogen storage material while also helping the development of the vdW corrections into DFT.

The present work demonstrates the utility and benefit of having DMC as a reliable benchmark, using the H<sub>2</sub> on SiCNT as the model system. SiCNT is one of the more promising candidate materials, having suitable bond length with better adsorbance than CNT. It is also often used for benchmark given the variability of its binding energy with regard to the chosen exchange-correlation functional. The plain local density approximation and generalized gradient model was found to (predictably) be insufficient, with significant over-/under-estimation of the binding energy and inaccurate geometry. Tkatchenko-Scheffler pairwise correction and vdW-DF2 nonlocal functional were found to best approximate DMC energetics, within 0.25 kcal/mol of the predicted 1.370(106) kcal/mol binding energy, while the geometry were found to be best predicted by exchange-dipole model and DFT+D3. Charge density analysis revealed some nonlocal functionals to produce unphysical densities, but with seemingly no bearing on the optimized geometry. It is concluded that combinations of corrections should be used at different stages (geometry and energy) for the most accurate result.

**Keywords:** Hydrogen storage, SiCNT, van der Waals, *ab initio*, Diffusion Monte Carlo

# Acknowledgments

I would like to thank my supervisors, Prof. Ryo Maezono and Assoc. Prof. Kenta Hongo, for their advice and support provided during my PhD in JAIST. These include matters pertaining not only to the important scientific discussions, but also with regard to project (and sometimes life) management, which I think would be very useful even beyond this doctoral program. I would also like to thank Prof. Shogo Okada, which, although we rarely discuss technicalities, always spare his time when it matters. I would like to thank Asst. Prof. Kosuke Nakano for his enormous effort in decoding my cryptic writing in the minor research project, as well as indirectly sustaining my motivation to not quit this PhD. I would like to thank Dr. Andrea Tirelli at SISSA for his expertise and a lot of assistance in graph formalism. I would also like to express my gratitude to Dr. Anouar Benali and Dr. Hyeondeok Shin at Argonne National Laboratory, they provided a lot of assistance concerning QMCPACK and computing facilities at Argonne. We had nice dinners, lunches, and other events, where they keep my interest up with theoretical discussions on QMC. Even though it did not end up in any theoretical projects, I am still keeping my interest for future collaborations. I would also like to thank everyone else at Maezono Laboratory, research assistants and friends, whose I am sure we shared a lot of joy (and despair).

This work would not have been possible without the computational capabilities provided by both JAIST and Advanced Leadership Computing Facility at Argonne. I would like to extend my gratitude to those who keep these facilities running at their best.

I would like to thank my friends at JAIST, for keeping me from being a research zombie with zero social life. Now I understand that everyone have their dark days, too, and it is not a sufficient condition for ceasing to exist. There was a particular individual,

which I am sure is too shy to be named here, who however unintentional they might be, has lit my internal competitive fire again. Lastly, special thanks to my family, without them, I would not even reach this stage.

# Contents

<b>Abstract</b>	<b>i</b>
<b>Acknowledgments</b>	<b>ii</b>
<b>Contents</b>	<b>iv</b>
<b>List of Figures</b>	<b>vii</b>
<b>List of Tables</b>	<b>1</b>
<b>Chapter 1 Introduction</b>	<b>1</b>
1.1 Background . . . . .	1
1.1.1 Hydrogen storage . . . . .	1
1.1.2 Materials informatics . . . . .	3
1.2 Motivation . . . . .	4
1.3 Problem Statement . . . . .	5
1.4 Outline . . . . .	5
<b>Chapter 2 Theoretical Framework</b>	<b>6</b>
2.1 Many-body Schrödinger equation . . . . .	6
2.2 Born-Oppenheimer Approximation . . . . .	8
2.3 Variational Method . . . . .	10
2.4 Hartree-Fock equations . . . . .	11
2.4.1 Basis sets . . . . .	13

2.5	Density Functional Theory . . . . .	15
2.5.1	Exchange-correlation functionals . . . . .	16
2.5.2	DFT and vdW interaction . . . . .	17
2.6	Quantum Monte Carlo methods . . . . .	21
2.6.1	Variational Monte Carlo . . . . .	21
2.6.2	Diffusion Monte Carlo . . . . .	23
<b>Chapter 3 Systems and Methods</b>		<b>26</b>
3.1	Structural Optimization . . . . .	26
3.1.1	Forms of SiC . . . . .	26
3.1.2	Structural optimization of $\beta$ -SiC . . . . .	27
3.1.3	Structural optimization of SiCNT . . . . .	30
3.1.4	Structural optimization of H <sub>2</sub> on SiCNT . . . . .	35
3.2	Binding energy evaluation . . . . .	41
3.3	DFT calculations . . . . .	42
3.4	VMC calculations . . . . .	43
3.5	Trial wavefunction optimization . . . . .	44
3.6	DMC calculations . . . . .	44
<b>Chapter 4 Results</b>		<b>46</b>
4.1	DMC binding energy estimation . . . . .	46
4.1.1	Effect of vacuum size . . . . .	46
4.1.2	DMC binding energy . . . . .	47
4.2	DFT binding energy estimation . . . . .	52
4.3	Charge density analysis . . . . .	55
<b>Chapter 5 Discussion</b>		<b>57</b>
5.1	DMC-DFT discrepancy . . . . .	57
5.2	Finite size error and timestep bias . . . . .	59
5.3	Geometry variance with different functionals . . . . .	60
<b>Chapter 6 Summary</b>		<b>66</b>
<b>References</b>		<b>68</b>



<b>List of Abbreviations</b>	<b>79</b>
<b>Biography</b>	<b>79</b>

# List of Figures

1.1	Comparison of volumetric and gravimetric energy density between known energy carriers. . . . .	2
3.1	Various arrangements of $sp^2$ planar SiCs and their associated nanotubes. . . . .	28
3.3	Chiral vector for classifying different SiCNT models. . . . .	31
3.2	Unit cell for periodic model of an armchair (5,5) SiCNT. . . . .	31
3.4	Cohesive energy vs. SiCNT diameter. . . . .	32
3.5	Cohesive energy vs. buckling radius. . . . .	33
3.6	Possible hydrogen binding sites on the SiCNT surface. . . . .	36
3.7	Parameters used to describe the $H_2$ conformation on the SiCNT surface. . . . .	36
3.8	Sites with significantly different post-optimization geometry. . . . .	40
3.9	Best-case binding energy comparison between possible adsorption sites on (5,5) SiCNT. . . . .	41
4.1	Total energy of simulation cell relative to vacuum depth. . . . .	47
4.2	Binding energy estimation from DMC. . . . .	52
4.3	Binding energy estimation from conventional DFT. . . . .	53
4.4	Binding energy estimation from energy-corrected DFT. . . . .	54
4.5	Binding energy estimation from nonlocal DFT. . . . .	55
4.6	Charge density difference $\Delta\rho(r)$ in the region near hydrogen adsorption site. . . . .	56
5.1	Binding energy vs. $H_2$ distance plot for various XCs. . . . .	58
5.2	DMC finite size correction for SiCNT-only fragment. . . . .	60

5.3	DMC finite size correction for SiCNT+H <sub>2</sub> complex, at (a) 2.20 Å, (b) 2.43 Å, (c) 2.83 Å, (d) 3.23 Å, (e) 3.63 Å, and (f) 5.00 Å distance. . . . .	61
5.4	DMC timestep extrapolations for H <sub>2</sub> . . . . .	61
5.5	DMC timestep extrapolations for SiCNT-only fragment with (a) 2×1×1, (b) 6×1×1, and (c) 8×1×1 supercell. . . . .	62
5.6	DMC timestep extrapolations for SiCNT+H <sub>2</sub> complex, at 2.20 Å distance with (a) 2×1×1, (b) 6×1×1, and (c) 8×1×1 supercell, and at 2.43 Å with (d) 2×1×1, (e) 6×1×1, and (f) 8×1×1 supercell. . . . .	62
5.7	DMC timestep extrapolations for SiCNT+H <sub>2</sub> complex, at 2.83 Å distance with (a) 2×1×1, (b) 6×1×1, and (c) 8×1×1 supercell, and at 3.23 Å with (d) 2×1×1, (e) 6×1×1, and (f) 8×1×1 supercell. . . . .	63
5.8	DMC timestep extrapolations for SiCNT+H <sub>2</sub> complex, at 3.63 Å distance with (a) 2×1×1, (b) 6×1×1, and (c) 8×1×1 supercell, and at 5.00 Å with (d) 2×1×1, (e) 6×1×1, and (f) 8×1×1 supercell. . . . .	63

# List of Tables

3.1	Calculated lattice parameter ( $a$ ), bulk modulus ( $B$ ), and cohesive energy ( $E_{\text{coh}}$ ) of $\beta$ -SiC. . . . .	30
3.2	Optimized geometries of SiCNTs using PBE exchange-correlation functional. . . . .	34
3.3	Optimized geometries of SiCNTs using PZ exchange-correlation functional. . . . .	34
3.4	Optimized conformation and adsorption energies of H <sub>2</sub> on the SiCNT surface. . . . .	38
4.1	DMC total energies per unit cell for every system, geometry, supercell, and timestep. . . . .	48
4.2	Timestep-extrapolated DMC total energies per unit cell for every system, geometry, and supercell. . . . .	50
4.3	Final DMC energies for every system and geometry. . . . .	50
5.1	Binding energy estimation for vs. vertical-oriented H <sub>2</sub> distance plot from DFT of all XCs and DMC. . . . .	59
5.2	H <sub>2</sub> conformations and adsorption energies from full geometry optimization. . . . .	65

# Chapter 1

## Introduction

### 1.1 Background

#### 1.1.1 Hydrogen storage

The word energy in colloquial use refers to a subset of its form which are immediately usable or are easily convertible into those that can be used for supporting human activities. In this age, it has become a foundation of the modern life, where artificial energy generation and usage is common typically in the form of electricity or hydrocarbons fuels. The importance of energy has spurred continuous research and development, with problems spanning from its generation, transport, and storage.

The increasing demand for clean, non-polluting, low emission energy sources has stimulated renewed interest in the problem of energy storage [1, 2]. Many of the renewable energy sources have fluctuating output, meaning that given the also variable demand, a form of energy storage mechanism is necessary, to store the excess and fill in the deficits. Additionally, in the transportation sector, it was found to be difficult to find an alternative to the fossil fuel with comparable energy density and convenience. Hydrogen energy is one of the compelling alternatives, along with other competitive technologies such as batteries. In general, the choice between battery and hydrogen largely depends on the required amount of stored energy given a volume or weight constraint, dictated by the mode of transport. Hydrogen is deemed more competitive on longer distance or higher capacity [3].

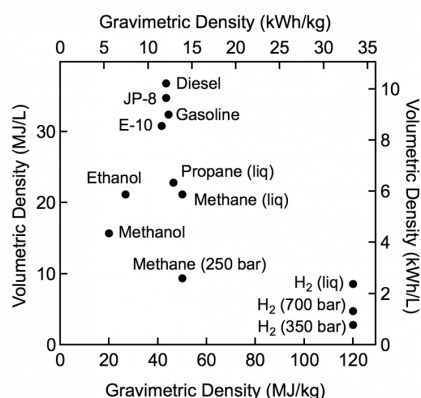


Figure 1.1: Comparison of volumetric and gravimetric energy density between known energy carriers. The figure was produced from calorimetry measurements included in a report by U.S. Department of Energy [4]

The problem with hydrogen is in its low volumetric energy density (Figure 1.1), making compact storage difficult without using very high pressure or very low temperature. This is especially problematic for automotive application, where both option compromises either cost and/or safety. On the other hand, hydrogen has high gravimetric energy density making it attractive for applications demanding minimized weight. To improve upon conventional storage technologies, developments of materials-enhanced hydrogen storages have been pursued, with alternatives including metal hydrides, adsorbent nanostructures, and chemical-based storages. The US Department of Energy has set target capacity at 7.5 %wt or 70 g/l for a viable commercial application [1]. Adsorbent nanostructures have lower energy lost in the adsorption cycle compared to alternatives, but the currently available materials have too weak binding energy, [2]. This lowers the adsorption capacity, while also restricting the possible environmental operating range, confining it to cryogenic use. In order to achieve higher-temperature adsorbent storage with higher capacity, further research into the possible material is necessary. This may include, among others, doping the structure with transition metals [5, 6], or by trying other nanostructure [7].

Silicon carbide nanotubes (SiCNT) is one of the nanostructures investigated for this purpose, with some theoretical and experimental studies predicted it to better adsorb H<sub>2</sub> relative to other candidates such as carbon nanotubes [8–10]. First reported in 2001 by Pham-Huu et al. [11] after a shape memory process using CNT as precursors combined

with vaporized SiO, several research groups have since reported its fabrication using various processes [12–21]. SiC in its bulk form is well known to have a high temperature and chemical resistance, as well as medium band gap, which if retained by the nanotube form, may allow for further application not possible using other nanostructures. Charge analysis from DFT studies revealed some charge transfer from the Si to C atom, creating surface dipoles even without transition metal doping [6, 8, 22–24]. The formation of surface dipoles has been ascribed to the increased hydrogen uptake of transition-metal-doped CNT, explaining the higher adsorption capacity [6, 25, 26].

### 1.1.2 Materials informatics

Approaches to materials simulation can traditionally be divided into two categories: model approaches, where empirical models are developed from macroscopic observations to directly solve practical problems, and *ab initio* simulations, where models are built upon fundamental physics theory, constructing the target system from the smallest unit. While the latter can be more accurate, particularly in edge or atypical cases, the computational cost is also much higher. This limits its initial application into smaller molecule and crystalline systems, or for tuning parameters of the model approaches.

In recent years, however, rapid development of massively parallel computing facilities and continuous improvements into the algorithm have allowed single point *ab initio* calculations to be performed in large number. With their output consist mostly of microscopic quantities, post-processing techniques have to be developed in order to obtain desirable macroscopic quantities directly comparable with the experiments. The fact that *ab initio* simulations is based on fundamental physics means, given appropriate trade-off between accuracy and cost, they can allow the search for hypothetical materials before their synthesis, guiding experimental efforts instead of just a confirmation and analysis tool.

Importing techniques from data science, applied into existing information from both simulations and experiments, material informatics is an emerging field with the aim to provide high-throughput, comprehensive, and reliable database for every existing and hypothetical materials. The diversity and flexibility of the available techniques means *ab initio* data can also be used to train the model, resulted in novel efforts such as separation of phases within powder XRD patterns by machine learning [27],

cycle performance estimation of batteries [28], and high-throughput search of polymers having high thermal conductivity [29]. Database of DFT data for many known materials has also been available [30]. To build an accurate model, the data point needs to be reliable, ideally accurate or at the very least have correctable systematic error. Thus, reducing computational cost to make it practical is no longer the main focus, *ab initio* simulations must also be increasingly accurate treating wide range of systems to support these efforts.

## 1.2 Motivation

DFT is the most popular method for studying material properties as it is perceived to have a balance between accuracy and cost. While perfectly adequate for bound system, systems with strong correlations or non-covalent interactions may cause it to fail. Pertinent to the studies of functional materials for hydrogen storage, particularly those based on nanostructures, is that the adsorption is dominated by vdW forces that has its origin on quantum fluctuation. Incorporating the effect coming of quantum fluctuation into conventional DFT framework is a challenging problem, leading to the development of correction schemes based on diverse physics. It is well known that these corrections can have varying accuracy or even diverging results depending on the system of study, therefore necessitating a reliable external calibration.

As a cutting-edge development, experimental data for these class of nanostructures for hydrogen storage are still limited. Furthermore, the expectation to develop more complex structures to achieve even better physical properties means increasing model size, rendering traditional “gold-standard” wavefunction methods like CCSD(T) to quickly become prohibitively expensive. Fixed-node diffusion Monte Carlo (FNDMC) offers a compelling alternative, as the vdW force is handled automatically by its many-body nature. It has also been proven to work well in treating dispersion, comparable to or sometimes better than the expensive CCSD(T) and CCSDT(Q) [31]. Unlike the latter, easy scaling and parallelization means FNDMC can be directly applied to larger system given sufficiently large computational resource. Therefore, DMC is a good candidate for supporting tuning of DFT even on novel system, reducing the need for experimental data expanding the frontier of materials informatics.



## 1.3 Problem Statement

The present work focuses on the origin and resolution of biases when using *ab initio* methods, in particular DFT, to estimate molecular adsorption properties in hydrogen storage materials, taking the advantage of FNDMC. Recent vdW correction schemes into DFT are benchmarked, including those utilizing pairwise potential as well as the non-local exchange-correlations. Adsorption curve and charge density are used as the main measure of accuracy, while also considering geometry optimizations resulting from the corrections. The present work also clarifies some aspects regarding the workflow and best practices on applying DMC on real system, as the different approach required relative to DFT means that the method still see limited use outside of QMC communities.

## 1.4 Outline

This dissertation is organized into six chapters.

- Chapter 1 provides the background of this work, including the state and difficulties of simulating hydrogen storage materials, with prospective outlook to material informatics.
- Chapter 2 gives the basis of *ab initio* simulation of material properties, mainly that of DFT and DMC.
- Chapter 3 details the target system and technical details on how to operate and process data from the simulations.
- Chapter 4 presents the results of the simulations including the binding energy estimations from both DMC and DFT as well as the charge densities.
- Chapter 5 elaborates the previous chapter by examining the discrepancy between DMC and DFT results, quantifying the biases to the DMC data, and the effect of exchange-correlation functionals into optimized geometries.
- Chapter 6 concludes the main result of the research including recommendations for future studies.

# Chapter 2

## Theoretical Framework

### 2.1 Many-body Schrödinger equation

Behavior of physical objects in the atomistic scale is subject to the law of quantum mechanics. Coming from the Greek word *quanta*, also related to the word *quantity* in English, it comprised a meaning of discrete steps, in opposition to continuous models common around the time of its early discovery. Its beginning was triggered by the observations of discrepancy in the ultraviolet region of black body emission, so-called ultraviolet catastrophe. The solution to this problem was to limit the allowed electromagnetic energy in the packet of  $E = nh\nu$ ,  $n$  being some integer, introduced by Max Planck, for which the  $h$  constant itself was then subsequently known by his name. His theory was not widely approved before the later independent discovery of photoelectric effects.

The field of many-body physics often deal with the problem of obtaining collective value from the given system state. Classical system often has their states directly storable in a form of scalar, vector, or tensors, of which such conceptions are no longer unfamiliar in the modern age due to ubiquity of computers. Quantum states, however, are often defined as complex function, although the detail can depend on the specific formulation. The norm or square magnitude of these functions is typically interpreted as probability density, in contrast to the definitive classical states. Observable quantities are defined with operators applied upon these states, with sometimes rather unintuitive consequences. For example, position and momentum in quantum mechanics are not

commutative  $[\hat{x}, \hat{p}] = i\hbar$ , consequently their eigenfunctions are not compatible. In practice, this means a state with definite position will not have a definite momentum, and vice versa, this being known as the uncertainty principle.

Narrowing down into atomistic simulation, the quantum operator one most likely encounter is the Hamiltonian  $\hat{H}$ , with its eigenvalue  $E$  interpreted as the system's total energy. The Hamiltonian describes a quantum system's time evolution:

$$-i\hbar \frac{\partial |\Psi(t)\rangle}{\partial t} = \hat{H} |\Psi(t)\rangle \quad (2.1)$$

Written in the above form, it is known as the Schrödinger equation. Here it is said to be written in a general form, as the basis has not been specified. Most commonly, position basis is used, resulting in  $\langle \vec{r} | \Psi \rangle = \Psi(\vec{r}, t)$  with the pure states can be written as wavefunctions of time and space. The exact form of the Hamiltonian is defined by the physical system, but for most purpose it is a combination of kinetic and some other potential:

$$\hat{H} = -\frac{\hbar^2}{2m} \nabla^2 + V \quad (2.2)$$

here  $\hbar$  is the reduced Planck constant, related to  $h$  by  $\hbar = h/2\pi$ , and  $m$  being the mass of some particle that is part of the system. For many-body systems, often the Hamiltonian will form into a summation, either of one-body terms or two and more-body interaction terms.

With the quantum states one typically found in atomistic simulation, it is reasonable to assume that it is separable into a product of time and spatial function, such as  $\Psi(\vec{r}, t) = \psi(\vec{r})\varphi(t)$ , allowing the equation to also be separable into the time-only and time-independent equation:

$$i\hbar \frac{1}{\varphi(t)} \frac{d\varphi(t)}{dt} = E \quad (2.3)$$

$$-\frac{\hbar^2}{2m} \nabla^2 \psi(\vec{r}) + V\psi(\vec{r}) = E\psi(\vec{r}) \quad (2.4)$$

The latter is the well-known time-independent Schrödinger equation. Since the left side of the equation is analogous to the original Hamiltonian, it is also possible to rewrite it into:

$$\hat{H}\psi(\vec{r}) = E\psi(\vec{r}) \quad (2.5)$$

thus making it clear that the separation constant  $E$  is the eigenvalue of the Hamiltonian. In many cases, it is sufficient to solve this reduced equation to obtain the total energy of a system, as long as there are only weak coupling between the temporal and spatial part. Many properties of interest in an atomistic system can be derived accurately enough from this total energy. Since it is an eigenvalue problem, the solution space for  $E$  is not a singular value, but rather a set of possible  $\{E_n\}$  and their associated eigenfunctions  $\{\psi_n(\vec{r})\}$ . This fact will be important in the next discussion on the variational theorem.

Physical system described in an atomistic simulation typically consisted of electrons in the field of atomic nuclei. The atomic nuclei, which is formed by several protons and neutrons, is often assumed as a single mass  $M$  with the charge  $Z$  depending on how many protons there are. Electrons and the nuclei interacts through Coulomb interaction, with each has their own kinetic energies. Therefore, the full Hamiltonian for the atomic system is:

$$\hat{H} = -\frac{1}{2} \sum_I \frac{1}{m_I} \nabla_I^2 - \frac{1}{2} \sum_i \nabla_i^2 + \sum_{I,J} \frac{Z_I Z_J}{|\vec{r}_{IJ}|} - \sum_{I,i} \frac{Z_I}{|\vec{r}_{Ii}|} + \sum_{i,j>i} \frac{1}{|\vec{r}_{ij}|} \quad (2.6)$$

where here the reduced form using atomic units such that  $m_e, \hbar, e = 1$  was used to simplify writing.  $I$  and  $i$  as indices for the nuclei and electrons.

## 2.2 Born-Oppenheimer Approximation

In Born-Oppenheimer approximation [32], the nucleus are treated as stationary objects, effectively reducing them to potential field from the viewpoint of the electrons. This approximation is reasonable due to the fact that a nucleus is more than 1000 times heavier than electrons (depends on atomic species), resulting in its much slower dynamics. The motivation for developing the approximation is to reduce computational cost, which can already be prohibitively expensive even for a tiny system. Akin to the previous separation, here the total wavefunction is assumed to be again separable into a product of electronic and nuclear wavefunction:

$$\Psi(\vec{R}, \vec{r}) = \phi_N(\vec{R}) \psi_e(\vec{r}, \vec{R}) \quad (2.7)$$

The electronic wavefunction is still dependent on the nuclear coordinate, thus written as  $\vec{R}$ , the dependency itself entered through the potential  $\sum_I Z_I/|\vec{r}_{Ii}|$ . Applying the Hamiltonian resulted in two equations separated for the electronic and nuclear wavefunctions:

$$\left( -\frac{1}{2} \sum_i \nabla_i^2 - \sum_{I,i} \frac{Z_I}{|\vec{r}_{Ii}|} + \sum_{i,j>i} \frac{1}{|\vec{r}_{ij}|} \right) \psi(\vec{r}; \vec{R}) = E_e(\vec{R}) \psi(\vec{r}; \vec{R}) \quad (2.8)$$

$$\left( -\frac{1}{2} \sum_I \frac{1}{m_I} \nabla_I^2 + E_e(\vec{R}) + \sum_{I,J>I} \frac{1}{|\vec{r}_{IJ}|} \right) \phi(\vec{R}) = E_{\text{tot}} \phi(\vec{R}) \quad (2.9)$$

where in the latter the solution (total energy) from the first equation entered statically for every term in the electronic summation. Both equation can now be independently solved to obtain the total energy, resulting in much lower computational costs due to the reduced number of matrix elements. This is only possible by ignoring nuclear coordinate dependence of the kinetic term when solving the electronic wavefunction, solving it at fixed  $R$ . Applying chain rule ( $\nabla^2(fg) = \nabla^2 f + \nabla^2 g + 2\nabla f \nabla g$ ) on the nuclear kinetic term resulted in:

$$\begin{aligned} -\frac{1}{2} \sum_I \frac{1}{m_I} \nabla_I^2 (\phi(\vec{R}) \psi(\vec{r}; \vec{R})) &= -\frac{1}{2} \sum_I \frac{1}{m_I} \psi(\vec{r}; \vec{R}) \nabla_I^2 \phi(\vec{R}) \\ &\quad - \frac{1}{2} \sum_I \frac{1}{m_I} (2\nabla_I \phi(\vec{R}) \nabla_I \psi(\vec{r}; \vec{R}) + \phi(\vec{R}) \nabla_I^2 \psi(\vec{r}; \vec{R})) \end{aligned} \quad (2.10)$$

While the first term is always evaluated as a part of the total wavefunction equation, the terms containing a gradient and second-order gradient of the electronic wavefunction with regard to the nuclei coordinates are ignored in the Born-Oppenheimer approximation. In general, it is a reasonable simplification since changes in the electronic wavefunction caused by the nuclei movement are generally small, unless when the nuclei are moving in a speed comparable to the electrons such as can be found in plasma physics.

## 2.3 Variational Method

A variational method have a property such that the expectation value of an operator, given any approximate solution, is always on the upper bound of the value given by exact solution. For example, when applied to the Hamiltonian, a variational method will have the property of:

$$\frac{\langle \Psi_T(\alpha) | \hat{H} | \Psi_T(\alpha) \rangle}{\langle \Psi_T(\alpha) | \Psi_T(\alpha) \rangle} \geq \frac{\langle \Psi | \hat{H} | \Psi \rangle}{\langle \Psi | \Psi \rangle} = E_0 \quad (2.11)$$

for some trial  $|\Psi_T(\alpha)\rangle$  state/wavefunction, which was made to depend on some parameters  $\alpha$ . By updating the parameter  $\alpha$ , the exact wave function  $|\Psi\rangle$  is approximated. Any methods such that this inequality does not apply is not variational. For methods that do, the problem of finding the ground state (and its energy) becomes a minimization problem:

$$\min_{\alpha} \frac{\langle \Psi_T(\alpha) | \hat{H} | \Psi_T(\alpha) \rangle}{\langle \Psi_T(\alpha) | \Psi_T(\alpha) \rangle} \quad (2.12)$$

As an example, suppose that the time-independent Schrödinger equation is used. Since it is an eigenvalue equation, for every  $\hat{H} |\Psi_a\rangle = E_a |\Psi_a\rangle$ , there will be a set of eigenvector/state/wave function  $|\Psi_a\rangle$ , where  $a = 0, 1, 2, \dots$ , with eigenvalue of  $E_0 \leq E_1 \leq \dots$ . There is no specific importance as to which state number has the lowest energy, just that they can be ordered. The lowest eigenvalue  $E_0$  and its associated eigenfunction  $|\Psi_0\rangle$  is called the ground state of the system. Since Hamiltonian operator is Hermitian, its eigenfunctions are orthonormal:

$$\begin{aligned} \langle \Psi_a | \Psi_a \rangle &= 1 \\ \langle \Psi_a | \Psi_b \rangle &= \delta_{ab} \end{aligned} \quad (2.13)$$

and due to the properties of Hilbert space on which quantum states are defined, these states can be expanded by a set of orthonormal basis vectors:

$$|\Psi_T\rangle = \sum_a c_a^T |\Psi_a\rangle \quad (2.14)$$

The coefficients to this expansion can be found from  $c_a^T = \langle \Psi_a | \Psi_T \rangle$ , any may be

interpreted as a ‘‘component’’ of the state in that basis. If the original state is normalized, i.e.,  $\langle \Psi_T | \Psi_T \rangle = 1$ , then

$$\begin{aligned} 1 &= \sum_{a,b} c_a^{T\dagger} c_b^T \langle \Psi_a | \Psi_b \rangle \\ &= \sum_a |c_a^T|^2 \end{aligned} \quad (2.15)$$

Applying the Hamiltonian to this normalized state:

$$\begin{aligned} E_T &= \langle \Psi_T | \hat{H} | \Psi_T \rangle = \sum_a \langle \Psi_a | c_a^{T\dagger} \hat{H} \sum_b c_b^T | \Psi_b \rangle \\ &= \sum_{a,b} E_b c_a^{T\dagger} c_b^T \langle \Psi_a | \Psi_b \rangle \\ &= \sum_a E_a |c_a^T|^2 \end{aligned} \quad (2.16)$$

If the lowest energy component is written separately, the below inequality is satisfied:

$$E_T = E_0 \sum_a |c_a^T|^2 + \sum_a (E_a - E_0) |c_a^T|^2 \geq E_0 \sum_a |c_a^T|^2 = E_0 \quad (2.17)$$

Put in other words, the energy (eigenvalue) of a trial, approximate, wavefunction always contains higher energy components, putting it in the upper bound of the exact ground state. The applicability of variational theorem forms the basis of many common approaches in solving the Schrödinger equation, including HF, DFT, VMC, and DMC. In methods where variationality is not guaranteed, for example when perturbation is considered, lower energy does not guarantee correctness, thus method other than minimization should be used.

## 2.4 Hartree-Fock equations

The Hartree-Fock approximation is a set of procedures including the Born-Oppenheimer approximation, a single Slater determinant to introduce antisymmetry into the wavefunction, and electron-electron interaction in an effective mean-field. To explain the use of determinant, first suppose that the wavefunction can be written as a product state of

single-particle states:

$$\Psi(\vec{r}_1, \vec{r}_2, \dots, \vec{r}_n) = \prod_n \phi_n(\vec{r}_n) \quad (2.18)$$

where the  $\vec{r}_n$  are single electron coordinate (3-dimension). Electrons are fermions, which should be indistinguishable and antisymmetric. This form achieves the indistinguishability as exchanging two positions resulted in the same wavefunction, but not the antisymmetry, as the sign of the wavefunction is not changed. By using a determinant (here flatly written using  $\varepsilon(i)$ , which assumes the value of 1 or  $-1$  depending on the parity of permutation operator  $P$ ):

$$\Psi(\vec{r}_1, \vec{r}_2, \dots, \vec{r}_n) = \frac{1}{\sqrt{N!}} \sum_P \varepsilon(i_1, i_2, \dots, i_n) \hat{P} \prod_n \phi_n(\vec{r}_{i_n}) \quad (2.19)$$

it is assured that the sign is inverted by a single exchange, hence consistent with the fermion behaviour. The normalization factor  $1/\sqrt{N!}$  came from the fact that there are  $N!$  amounts of possible permutations.

Applying Lagrange multipliers to the original problem with the previous wavefunction form, the problem is reduced into what is being known as the Hartree-Fock equations:

$$\left( -\frac{1}{2} \nabla_i^2 - \sum_I \frac{Z_I}{|\vec{r} - \vec{R}_I|} \right) \phi_i(\vec{r}) + \sum_j \int d\vec{r}' |\phi_j(\vec{r}')|^2 \frac{1}{|\vec{r} - \vec{r}'|} \phi_i(\vec{r}) - \sum_j \int d\vec{r}' \phi_j^*(\vec{r}') \frac{1}{|\vec{r} - \vec{r}'|} \phi_i(\vec{r}') \phi_j(\vec{r}) = \varepsilon_i \phi_i(\vec{r}) \quad (2.20)$$

This equation is analogous to the Schrödinger equation, but applies to the individual single-particle orbitals instead on the whole wavefunction. If written as a single operator, the left-hand side is called the Fock operator  $\hat{F}$ . The  $i$  index sums over all static potentials (nuclei), while the  $j$  sums over all orbitals, thus all electrons. The last integral is the *exchange* term, which does not appear if the symmetrical product (Hartree) was used instead. Upon solving the equation,  $\varepsilon$  is obtained as the value of the Lagrange multipliers. It is related to the total energy of the system by summing all of the multipliers, plus the value of one-body part within the Fock operator, i.e., excluding the Coulomb (first integral term) and the exchange integral. As a single orbital is solved



at a time, with others held constant, each effectively interact only through their mean field. In practice, the equation is iteratively solved until self-consistency is achieved, i.e., when the multipliers converged to a value.

### 2.4.1 Basis sets

A common configuration for the single-particle orbitals is the sum of basis functions:

$$\psi_n(\vec{r}) = \sum_m c_{mn} \varphi_m(\vec{r}) \quad (2.21)$$

where  $\varphi_m(\vec{r})$  is the basis function multiplied by some scalar  $c_{mn}$ . Different to the expansion of Hilbert space states, here the basis are not necessarily orthogonal with each other. Common choices are plane waves, gaussians, slater functions (atomic orbitals), and particularly for QMC use, b-splines (blip). Each of these choices have their own merits.

Gaussian basis sets are mathematically elegant with analytic products, derivatives, and several other operations. Therefore, in general it requires fewer terms for a similar accuracy. Periodicity is not inherent, unlike with plane waves, eliminating the need for adding vacuum. With gaussians, however, there are many possible sets for every element, without systematic improvement to accuracy in general. In relevance to the QMC, it also failed to produce cusp at the core without explicit corrections. On the other hand, slater functions do not have the last problem, but also the computational benefits of gaussians.

For periodic system, plane wave is often chosen as the solution of Schrödinger equation for electron in vacuum is sum of plane waves, plus modulation by periodic potential (Bloch theorem) in the presence of a periodic potential such as in crystalline/periodic system:

$$\psi_k(\vec{r}) = e^{i\vec{k}\cdot\vec{r}} \cdot u(\vec{k}, \vec{r}) \quad (2.22)$$

Due to its inherent periodicity, it is somewhat less suitable for modelling molecules (needs empty space to avoid image interaction). Compared to gaussian, it is more general, meaning that there is no need for choosing a specific set, and can be systematically

improved by adding more functions. The orbital expansion in plane waves is:

$$\psi_n(\vec{r}) = \sum_k c_{nk} e^{i\vec{k}\cdot\vec{r}} \quad (2.23)$$

summed over some wave vectors  $\vec{k}$ . If the reciprocal vector  $\vec{G}$  is also considered, the orbitals are then be expanded as:

$$\begin{aligned} \psi_{nk}(\vec{r}) &= e^{i\vec{k}\cdot\vec{r}} \sum_G c_{nkG} e^{i\vec{G}\cdot\vec{r}} \\ &= \sum_G c_{nkG} e^{i(\vec{G}+\vec{k})\cdot\vec{r}} \end{aligned} \quad (2.24)$$

The wave vector  $\vec{k}$  can be chosen to reside within simulation cell's Brillouin zone by folding. The previously mentioned systematic improvement is then performed by increasing the number of allowed plane-waves within an energy cutoff  $|\vec{k} + \vec{G}|^2$ . In general, however, pseudopotentials or effective core potentials are used together with plane waves, as a lot of waves will be required for drawing the core region with their larger localized fluctuations.

In QMC, particularly VMC and DMC, due to the need for evaluating local energy and wavefunction ratio, delocalized basis sets like plane waves are not computationally efficient. Therefore, it is customary to re-project plane waves into another, localized basis prior to the calculation. One popular choice is the b-spline ‘‘blip’’ basis set first introduced by Alfe et al. [33]. Blip functions are cubic polynomials that is zero outside some specified bounding box. Each orbital will be in the form of

$$\psi_n(\vec{r}) = \sum_s a_{ns} \Theta_s(\vec{r}) \quad (2.25)$$

with  $a_{ns}$  scalar and  $\Theta_s$  in the form of

$$\Theta_s(\vec{r}) = \prod_{i=(x,y,z)} \phi((r_i - R_i)/a) \quad (2.26)$$

for some spatial cubic grid spacing  $a$  and spline centre  $R$ , with each  $\phi$  function defined

piecewise as

$$\phi(\varepsilon) = \begin{cases} 1 - \frac{3}{2}\varepsilon^2 + \frac{3}{4}\varepsilon^3, & 0 \leq |\varepsilon| \leq 1, \\ \frac{1}{4}(2 - |\varepsilon|)^3, & 1 < |\varepsilon| \leq 2, \\ 0, & |\varepsilon| > 2, \end{cases} \quad (2.27)$$

The coefficient of the splines itself can be obtained from the plane-wave coefficient by the below relation

$$a_{ns} = \sum_k c_{nk} \gamma_k e^{ik \cdot R} \quad (2.28)$$

with  $c, \gamma$  being the plane-wave coefficients.

## 2.5 Density Functional Theory

A completely separate method, density functional theory (DFT) attempts to solve the original problem by using density (of electron) as the basic variable. Compared to the wavefunction, density is only 3-dimension, instead of 3N-dimension of the original wavefunction, thus computationally beneficial. The present-day technique is based on the work of Hohenberg and Kohn [34], in which it is postulated that: 1. The external potential of Equation 2.30 is unique function of the density, and 2. the correct density is the one that minimizes the energy functional  $E[n]$ . Similar to the Hartree-Fock procedure, DFT involves iterative solution of a set of equations. In DFT, the wave function (from orbital) is obtained from the given density, and vice versa, together forming a self-consistent loop. Initial guess for the density can be obtained for example from superposition of atomic orbitals. For a Slater determinant, the density can be obtained from the orbitals through:

$$n(\vec{r}) = \sum_i |\phi_i(\vec{r})|^2 \quad (2.29)$$

which is then used to build the so-called Kohn-Sham (KS) potential:

$$V_{\text{KS}}(\vec{r}) = V_{\text{ext}}(\vec{r}) + \frac{\partial E_{\text{XC}}[n]}{\partial n(\vec{r})} + \int n(\vec{r}') \frac{1}{|\vec{r} - \vec{r}'|} d\vec{r}' \quad (2.30)$$

This KS potential is in turn used to obtain the orbitals by

$$\left(-\frac{1}{2}\nabla^2 + V_{\text{KS}}(\vec{r})\right)\phi_i(\vec{r}) = \varepsilon_i\phi_i(\vec{r}) \quad (2.31)$$

By optimizing the parameter in the orbitals to lower the energy, a solution is obtained. Within the KS potential,  $E_{\text{XC}}$  is the exchange-correlation energy, describing all interactions between the electrons in the system. While the existence of a potential exactly solving the original problem is mathematically guaranteed, the actual form is not known, resulting in many different approximations existing today. Finally, total energy of the system can be obtained from:

$$E = \sum_i \varepsilon_i - \frac{1}{2} \int n(\vec{r}) \frac{1}{|\vec{r} - \vec{r}'|} n(\vec{r}') d\vec{r} d\vec{r}' + E_{\text{XC}}[n] - \int V_{\text{XC}}[n(\vec{r})]n(\vec{r}) d\vec{r} \quad (2.32)$$

### 2.5.1 Exchange-correlation functionals

Fundamental in determining the accuracy of a DFT work, many approximations exist for the XC potential, combining different physics and tuned to some fundamental or specific target systems. The terms of the XC potential can generally be written as a linear combination:

$$E_{\text{XC}} = E_{\text{X}} + E_{\text{C}} + E_{\text{GX}} + E_{\text{GC}} + \dots \quad (2.33)$$

Listed here are the exchange ( $E_{\text{X}}$ ), correlation ( $E_{\text{C}}$ ), their gradient-dependent parts ( $E_{\text{GX}}$  and  $E_{\text{GC}}$ ), among others. Some implementation either developed completely new function for each term, or mixes in the previously developed term, calibrated to different base material.

The categorization of XC potentials generally is based on their relationship to the density: local density approximation (LDA), generalized gradient approximation (GGA, includes gradient corrections), hybrids (added some fractions of exact exchange), etc. For example, LDA is only a function of some density:

$$E_{\text{XC}}^{\text{LDA}}[n] = \int f(n_{\uparrow}, n_{\downarrow}) d\vec{r} \quad (2.34)$$

while GGA additionally dependent on the gradient of such density:

$$E_{XC}^{GGA}(n_{\uparrow}, n_{\downarrow}) = \int f(n_{\uparrow}, n_{\downarrow}, \nabla n_{\uparrow}, \nabla n_{\downarrow}) d\vec{r} \quad (2.35)$$

Many reference data from experiments or more accurate theoretical method is used to develop these potentials. For example, in the Perdew and Zunger LDA [35] that is used in this work, the terms are derived from calculation on uniform electron gas systems. The PBE [36] potential used to represent GGA in this work also similarly not specifically tuned to any particular system.

## 2.5.2 DFT and vdW interaction

The van der Waals interaction arises from quantum fluctuation, resulting in a temporary polarization of charge density correlating with another nearby charge density creating the weak attraction/repulsion. Due to this nature, non-local terms are required to describe the effect, which is not included by the conventional LDA- or GGA- DFT. This resulted in poor accuracy of the estimated binding energies [31]. To address this, diverse schemes from varying physics have been developed, among them two categories can be recognized: 1. pairwise potential expanding  $r^{-6}$ ,  $r^{-8}$  and so forth, and 2. addition of non-local terms into the exchange-correlation functional based on 2<sup>nd</sup> perturbation. These approaches can prove to be accurate, however their empirical nature does not guarantee systematic improvement in the general accuracy.

In the pairwise potential approach, *ab initio* quantities including orbitals, charge density, and energies are left unchanged, thus the change to the potential energy surface is achieved by geometric dependency of the correction. The total system energy including the dispersion correction can be written in the form of:

$$E_{DFT} = E_{DFT} + E_{disp} \quad (2.36)$$

with the vdW correction written as a power series expansion of 2-body interactions:

$$E_{disp} = -\frac{1}{2} \sum_{ij} \sum_{n=6,8,10,\dots} \frac{C_{nij} f_n(r_{ij})}{r_{ij}^n} \quad (2.37)$$

The  $C_i$  term is often called the dispersion coefficient, which determine how strong is the dispersion between to atoms  $i$  and  $j$ . A damping function  $f$  is also often added to control the behaviour at close interatomic distance (i.e., for the binding atoms, as the corrections are applied to all atoms). The expansion is typically from  $r^{-6}$  (D2, TS) to  $r^{-10}$  (XDM) terms. How the dispersion coefficient and damping functions are defined is what differentiate the various pairwise models.

In DFT+D2 approach by Grimme et al. [37], the dispersion energy is in the form of:

$$E_{D2} = -\frac{1}{2} \sum_{ij} \frac{C_{ij}f(r_{ij})}{r_{ij}^6} \quad (2.38)$$

with the damping function  $f$  in the form of:

$$f(r_{ij}) = \frac{s}{1 + e^{-d(r_{ij}/R_{ij}-1)}} \quad (2.39)$$

The parameter  $s$  is the global scaling parameter, with the value dependent on the exchange-correlation functional the correction is applied on. The dispersion coefficient  $C_{ij}$  is calculated pairwise from  $\sqrt{C_{ii}C_{jj}}$  where each value are fixed according to element type. Likewise, distance parameter  $R_{ij}$  is also calculated from a fixed table by  $R_i + R_j$ . Therefore, the DFT+D2 correction is not sensitive to the local geometry nor the chemical environment of the adsorption site.

A further development by the same research group, DFT+D3 [38] added 3-body interaction term, higher order  $r^{-8}$  expansion to the 2-body term, and re-calculated the dispersion coefficient from *ab initio* results, among others. Thus, the dispersion energy can be written as:

$$E_{D3} = E^{(2)} + E^{(3)} \quad (2.40)$$

The 2-body term with the added  $r^{-8}$  term is:

$$E^{(2)} = -\frac{1}{2} \sum_{ij} \frac{C_{6ij}f_6(r_{ij})}{r_{ij}^6} + \frac{C_{8ij}f_8(r_{ij})}{r_{ij}^8} \quad (2.41)$$

with the damping term now in the form of:

$$f(r_{ij}) = \frac{s_n}{1 + 6(r_{ij}/(s_{Rn}R_{ij}))^{\alpha_n}} \quad (2.42)$$

The distance parameter is also computed differently, with  $R_{ij} = \sqrt{C_{8ij}/C_{6ij}}$ , and adding a fixed/exchange-correlation dependent parameters  $s_{Rn}$  and  $\alpha_n$ . Unlike in DFT+D2, the dispersion coefficient  $C_{ij}$  is now dependent on the local coordination number, thus inserting a form of geometric dependency into the dispersion. The the 3-body term follows Axilrod-Teller-Muto model [39] with the previous damping term:

$$E^{(3)} = \sum_{abc} f_3(\bar{r}_{abc}) E_{abc} \quad (2.43)$$

$$E_{abc} = \frac{C_{abc}9(3 \cos \theta_a \cos \theta_b \cos \theta_c + 1)}{(r_{ab}r_{bc}r_{ca})^3} \quad (2.44)$$

The Tkatchenko-Scheffler method (TS) [40] is another type of modification to the DFT+D2, with the geometric dependence instead achieved through charge-density-dependent parameters. To be precise, the dispersion parameter between two species is combined by the way of:

$$C_{ij} = \frac{2C_{ii}C_{jj}}{\frac{\alpha_j}{\alpha_i}C_{ii} + \frac{\alpha_i}{\alpha_j}C_{jj}} \quad (2.45)$$

with a new atom-dependent parameter  $\alpha$ . The charge-density-dependency is achieved by scaling of  $\alpha$ ,  $C$ , and  $R$  by the effective volume  $v_i$ :

$$\alpha_i = v_i \alpha_i^{\text{free}}, \quad (2.46)$$

$$C_{ii} = v_i^2 C_{ii}^{\text{free}}, \quad (2.47)$$

$$R_i = (\alpha_i/\alpha_i^{\text{free}})^{(1/3)} R_i^{\text{free}}. \quad (2.48)$$

where the “free” values are fixed for each species. The connection to the density comes from the calculation of the effective volume, which comes from Hirshfeld partitioning [41]

$$v_i = \frac{\int r^3 w_i(\vec{r}) n(\vec{r}) d^3 \vec{r}}{\int r^3 n_i^{\text{free}}(\vec{r}) d^3 \vec{r}} \quad (2.49)$$

with the Hirshfeld weights  $w_i(\vec{r})$  also density-dependent by

$$w_i(\vec{r}) = \frac{n_i^{\text{free}}(\vec{r})}{\sum_j n_j^{\text{free}}(\vec{r})} \quad (2.50)$$

The combined distance parameter  $R_{ij}$  identical to DFT+D2's definition.

Exchange-hole dipole moment (XDM) [42] is distinct from the other pairwise model by the fact that its dispersion coefficient  $C$  is calculated from an exchange hole model over the SCF density. This is in contrast to the pre-calculated coefficients in other model. Therefore, the dispersion also has geometrical dependency through density, similar to TS. The damping function contains an additional ‘‘van der Waals radii’’  $R_{\text{vdW},ij}$  term

$$f = \frac{R_{ij}^n}{R_{ij}^n + R_{\text{vdW},ij}^n} \quad (2.51)$$

defined as

$$R_{\text{vdW},ij} = \frac{1}{3} \left( \left( \frac{C_{8ij}}{C_{6ij}} \right)^{1/2} + \left( \frac{C_{10ij}}{C_{6ij}} \right)^{1/4} + \left( \frac{C_{10ij}}{C_{8ij}} \right)^{1/2} \right) \quad (2.52)$$

Note that here up to  $r^{-10}$  expansion is used, so the final form becomes

$$E_{\text{XDM}} = -\frac{1}{2} \sum_{i,j=1}^{N_{\text{at}}} \frac{C_{6ij} f(r_{ij})}{r_{ij}^6} + \frac{C_{8ij} f(r_{ij})}{r_{ij}^8} + \frac{C_{10ij} f(r_{ij})}{r_{ij}^{10}} \quad (2.53)$$

With the nonlocal vdW corrections, the dispersion energy is instead calculated as a part of the SCF energy. The word ‘‘nonlocal’’ comes from the fact that their calculation includes the evaluation of a two-center integral. This nonlocal term is introduced into the correlation functional:

$$E_{\text{C}}[n] = E_{\text{C}}^0[n] + E_{\text{C}}^{\text{nl}}[n] \quad (2.54)$$

with the first term  $E^0$  being the local part of the correlation. The nonlocal correlation has the general form of:

$$E_{\text{C}}^{\text{nl}} = \frac{1}{2} \int n(\vec{r}) K(\vec{r}, \vec{r}') n(\vec{r}') d\vec{r} d\vec{r}' \quad (2.55)$$

which basically expresses the interaction between two density points in space, with the



interaction detail described by the  $K$  integration kernel. The difference between different kinds of nonlocal functional is in the form of this kernel.

For the vdW-DFx [43, 44] family, this kernel takes the form of

$$K_{\text{vdW-DFx}} = \frac{2me^4}{\pi^2} \iint_0^\infty a^2 b^2 W(a, b) T(v(a), v(b), v'(a), v'(b)) da db \quad (2.56)$$

where  $a$  and  $b$  are two dummy variables, with the whole kernel ultimately dependent on  $\vec{r}$  and  $\vec{r}'$  through the  $v$  and  $v'$  quantities, with their detailed formula left at the original reference. Ultimately, this kernel was developed from polarization model of plasma oscillation. The difference between the original vdW-DF and vdW-DF2 is in the choice of exchange functional: revPBE [45] instead of PW86 [46], thus accordingly changes some parameters within the model. The argument was that revPBE can incur spurious binding, as well as being too repulsive. It was developed to improve overestimation of the binding geometries in some cases with the original vdW-DF.

The rVV10 [47] takes a different approach with the kernel in the form of:

$$K_{\text{rVV10}} = -\frac{3e^4}{2m^2} \frac{1}{(qR^2 + 1)(q'R^2 + 1)(qR^2 + q'R^2 + 2)} \quad (2.57)$$

Here,  $\vec{r}$  and  $\vec{r}'$  dependencies are inserted through  $R$ , which is defined as  $R = |\vec{r}' - \vec{r}|$ . The form is noticeably simpler than the vdW-DFx, and like vdW-DF2, it also utilized PW86 for the exchange. The original paper reported it to improve geometry prediction over vdW-DF2 which tend to overestimate binding distance in some molecules and underestimate bulk modulus.

## 2.6 Quantum Monte Carlo methods

### 2.6.1 Variational Monte Carlo

Variational Monte Carlo employs variational theorem together with Monte Carlo integration (with random sampling) to obtain the expectation of some observable given an operator:

$$\langle o \rangle = \frac{\langle \Psi_T(\alpha) | \hat{O} | \Psi_T(\alpha) \rangle}{\langle \Psi_T(\alpha) \rangle} \quad (2.58)$$

Here,  $\langle o \rangle$  is the expected value for some quantum operator  $\hat{O}$  applied to some trial state  $|\Psi_T\rangle$ . The trial state is made to be dependent on some parameter  $\alpha$ , so as to be able to varied with the objective of minimizing  $o$ . This is because in a variational method (Section 2.3),  $o$  will be in the upper bound of the exact eigenvalue. Theoretically, if the state or wavefunction happened to match one of the eigenfunctions for the operator  $\hat{O}$ , the observable will assume a constant value (zero variance), with  $o$  coincides with the operator's eigenvalue. Otherwise, it should assume a variance of  $\langle o^2 \rangle - \langle o \rangle^2$ .

The Monte Carlo integration is used for evaluating the expectation values. It is based on the principle that:

$$I = \int f(\vec{r}) d\vec{r} \approx \frac{1}{N} \sum_n f(\vec{r}_n) \quad (2.59)$$

as the sum (random sampling) gets larger (m) infinity. Each  $\vec{r}_n$  is a single sampling point. To see how this integral is connected with the original problem, note that  $f(\vec{r})$  can be multiplied by some  $\rho(\vec{r})/\rho(\vec{r})$  without changing its value:

$$I = \int \rho(\vec{r}) \frac{f(\vec{r})}{\rho(\vec{r})} d\vec{r} \quad (2.60)$$

Suppose that this  $\rho(\vec{r})$  is a probability density with the property of  $\int \rho(\vec{r}) d\vec{r} = 1$ . By also inserting  $\Psi_T^{-1} \Psi_T$  to the original problem (Equation 2.58),

$$\langle E \rangle = \frac{\int |\Psi_T(\vec{r})|^2 \Psi_T^{-1}(\vec{r}) \hat{H} \Psi_T(\vec{r}) d\vec{r}}{\int |\Psi_T(\vec{r})|^2 d\vec{r}} \quad (2.61)$$

where the previously described probability density corresponds to the  $(|\Psi_T|^2 / \int |\Psi_T|^2)$ . The quantity  $(\Psi_T^{-1} \hat{H} \Psi_T)$  is also local energy, because it matches the expected energy for its given local configuration. Efficient sampling is achieved when  $\rho(\vec{r})$  was made to somewhat approximates  $f(\vec{r})$ .

The present work is not concerned with the variety and merits of available random number generators, but it suffices to say that generating a non-uniform distribution is not trivial. Most QMC codes employs the so-called Metropolis algorithm. Based on Markov chains, the random number is regarded as the state, with probabilistic accept-reject step for generating the next random state / number. Metropolis algorithm can generate any

kind of probabilistic distribution, but needs to be run first for a certain number of steps (the *equilibration* or *warm up* period). The probabilistic transition needs to satisfy the detailed balance condition:

$$\sum_r \omega_{rr'} A_{rr'} \rho(\vec{r}, t) = \sum_{r'} \omega_{r'r} A_{r'r} \rho(\vec{r}', t) \quad (2.62)$$

One way to explain this condition is by considering before/after states (value of random number before/after a transition). Here, it is given by the  $\vec{r}$  and  $\vec{r}'$ , where instead of a single random number, a set of electron coordinates is used to match the implementations. Detailed balance means at equilibrium, the transition between any two states are symmetric. It does not necessarily equal to symmetric transition probability, however, as it is also affected by the equilibrium distribution. In Metropolis algorithm, the transition probability is divided into two parts,  $\omega$  and  $A$ , as step probability (probability for requesting  $\vec{r} \rightarrow \vec{r}'$  transition) and acceptance probability (whether the request is accepted or not). Transition probability is typically taken from some normal distribution. Acceptance probability is set to 1 (always accept) when the target probability density at the destination is larger, and to the ratio of the before/after density otherwise. The combination of variational theorem, Monte Carlo integration, and the Metropolis method, describes VMC.

## 2.6.2 Diffusion Monte Carlo

Diffusion Monte Carlo (DMC) is conceptually distinct from VMC, although they are related by the sampling of some trial function to obtain the expectation value of a quantum operator. Unlike VMC, where the sampling distribution follows the magnitude of given trial function, DMC distributes the sample by a propagator derived from the imaginary time Schrödinger equation. This means that while VMC is as accurate as the given wave function, DMC can effectively change the shape of the trial function without being limited by the degree of freedom of the given basis set. If the propagator is accurate, DMC can achieve higher accuracy than VMC. The evolution of the sampling point is best described by a Green function:

$$G(\vec{r} \leftarrow \vec{r}') = \langle \vec{r} | e^{-\tau(\hat{H}-E_T)} | \vec{r}' \rangle \quad (2.63)$$

derived initially from time-dependent Schrödinger equation. Imaginary time substitution ( $\tau = it$ ) allows the oscillating solution to instead turn into a decaying diffusion-like equation. Thus DMC actually describes how the system evolve with imaginary time, rather than real time of the original time-dependent Schrödinger equation:

$$\left(\hat{H}(\vec{r}) - E_T\right) \Psi(\vec{r}, \tau) = -\frac{\partial \Psi(\vec{r}, \tau)}{\partial \tau} \quad (2.64)$$

Lastly, trial energy  $E_T$  is customarily added to an offset.

Solving the above equation resulted in  $(\sum_a c_a \Psi_a \exp -(E_a - E_T)\tau)$ , highlighting the connection with Green function. With regard to the offset  $E_T$ , it has two functions. Firstly, when  $E_T$  is set to  $E_0$ , only states corresponding to the  $E_0$  energy remains, with the rest decays (higher  $E_n$  energy states decay faster). The second function is to control “walker” population in the practical implementation. Walkers are a set of independently evolving configuration, where in practice some thousands are used in a single run to avoid sampling bias.

As the Hamiltonian  $\hat{H}$  have both kinetic and potential terms, each being an operator where  $e^{(a+b)} = e^a e^b$  is not always true, the exact form of the Green function becomes technically unknown. This is true for most system of interest as the external potential exists in the form of ionic field. Practical implementation employed Trotter-Suzuki approximation to solve the problem:

$$e^{-\tau(\hat{T}+\hat{V})} \approx e^{-\tau\hat{V}/2} e^{-\tau\hat{T}} e^{-\tau\hat{V}/2} \quad (2.65)$$

This approximation has third degree error in the timestep variable, being only exact at zero timestep. Since zero timestep equal no evolution, in most DMC calculation, the total energy is either extrapolated from several DMC runs at different timestep sizes, or approximated by using small enough timestep.

The discussion up to this point assumes a positive-definite wavefunction (thus analogous to a probability density). For fermionic system where the wave function is signed, however, the treatment becomes more complex. So far, there are no practical implementation that can avoid sign problem without fixed node approximation. In fixed node approximation, each walker are kept in their own nodal pockets, keeping note of

their sign, crossing disallowed. This means that the accuracy of DMC can be affected by the quality of the input nodal surface, although for system where the interaction is dominated at the region with fewer nodes, such as vdW in this work, the error is often insignificant.

# Chapter 3

## Systems and Methods

### 3.1 Structural Optimization

#### 3.1.1 Forms of SiC

The most studied form of silicon carbide is the bulk form [48], where it is well known for having relatively large band gap (between 2.2–3.3 eV) as well as high temperature and chemical stability. These properties make it desirable for use in high power or high frequency electronic devices. Having either hexagonal or cubic symmetry, it is also known to exhibit polytypism, a special case of polymorphism limited to the hexagonal *c*-axis. One way to view this polytypism is by observing that there are two valid ways to stack the SiC tetragonal layers in the *c*-direction, each of these configurations at 180° opposite of each other. There are no known limits to the periodicity of this stacking, with some polytypes can have more than 20 layers of periodicity. The simplest of these polytypes is the known as the 3C or  $\beta$ -SiC, where its layer all align in the same direction, resulting in cubic symmetry similar to diamond.

Unlike carbon which were the first to be found forming various planar allotropes, it was only relatively recently that SiC was also found to have the similar ability. One possible explanation is that unlike C, which has relatively similar enthalpies between its 2-dimensional  $sp^2$  and 3-dimensional  $sp^3$  configuration [49, 50], silicon is known to prefer the 3-dimensional  $sp^3$  [22, 49], resulting in it energetically preferring the bulk form. Regardless, experimental studies have confirmed the possibility for the

formation of nanotube-shaped SiC, some were found to be distinct from its bulk phase [11, 18], while others instead synthesized nanotube-shaped  $\beta$ -SiCs [51, 52]. Molecular dynamics simulations predicted the nanotube shape to be more stable than nanowires at larger diameter [53], with melting temperature predicted to be around 1700 K or higher, comparable to that of bulk SiC [53–55]. In line with the enthalpy conjecture, it was indeed found to be less energetically favorable than the bulk  $\beta$ -SiC, however its strain was lower than CNT, meaning given a SiC sheet was successfully synthesized, it is more likely to morph into nanotubes than CNT is from graphites [50]. Possible synthesis of this SiC sheet has been experimentally observed in as early as 2017 [24].

The most often used model of SiCNT in atomistic simulations is analogous to the single-walled CNT, but with half of the carbon sites substituted by silicon [6–8, 22, 23, 49, 50, 56–65]. A study on various SiC nanotubes at non-1:1 stoichiometry suggested that structures with more than 50% Si is unstable, resulting in the collapse of the nanotube structure and formation of nanowires or three-dimensional clusters [22]. DFT structural optimization suggested the structure exhibits some buckling, with the Si and C atom residing at two different distances from the nanotube axis. This buckling was found to be less than 0.5 Å, and decreases with increasing nanotube diameter [57, 58, 65, 66]. In general, the 1:1 SiCNT can be constructed with either (Si-C) or (Si-Si + C-C) configuration, these often referred to as type-1 or type-2 SiC sheet (Figure 3.1). When folded into a nanotube, an additional type-3 SiCNT can also be constructed by folding the type-2 sheet at 60° degree relative to the type-2 SiCNT [56, 57]. The type-1 (Si-C) nanotube was found to be the most stable regardless of its diameter and chirality [56–58], therefore only type-1 SiCNT is considered in the present study.

### 3.1.2 Structural optimization of $\beta$ -SiC

The  $\beta$ -SiC with its cubic symmetry is the simplest of bulk SiCs, having only a single crystal parameter and two fixed atomic positions. As a result, its geometry optimization is relatively straightforward even when employing methods with no pressure implementation such as DMC, making it a good candidate to perform initial calibration of the DFT method. In particular, it is important to first confirm whether it is possible to obtain reliable geometries, even when the *beta*-SiC itself is constructed of the  $sp^3$  bonds instead of  $sp^2$  of the planar SiC and SiCNT.

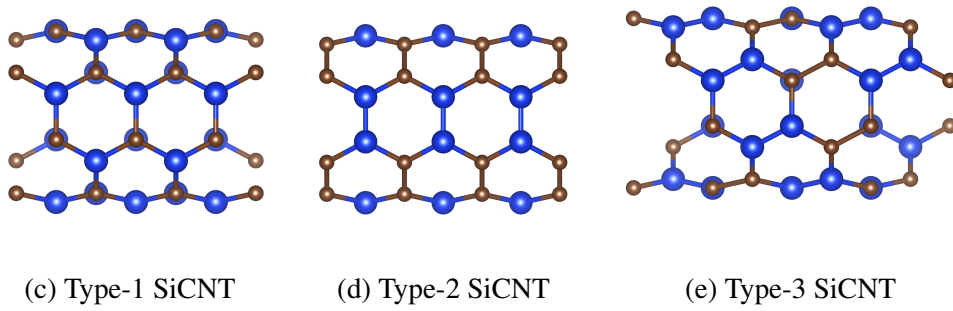
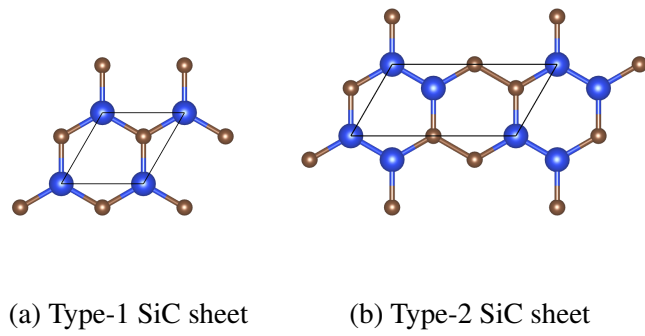


Figure 3.1: Various arrangements of  $sp^2$  planar SiCs and their associated (4, 4) nanotubes. Blue and brown spheres represents Si and C atoms, respectively, with the rectangles over the sheet SiCs indicating one of the possible primitive unit cells.



An equation of state fit was performed to obtain three physical properties: the single lattice parameter  $a$ , bulk modulus  $B$ , and cohesive energy  $E_{coh}$ , where experimental data for each of them are widely available. Vinet equation of state [67]:

$$E(V) = E_0 - \frac{4B_0V_0}{(B'_0 - 1)^2} \left( 1 - \frac{3}{2}(B'_0 - 1) \left( 1 - \frac{V}{V_0} \right)^{1/3} \right) \exp \left( \frac{3}{2}(B'_0 - 1) \left( 1 - \frac{V}{V_0} \right)^{1/3} \right) \quad (3.1)$$

was fitted to the total energies of several unit cells between  $-10\%$  and  $+10\%$  of the experimental volumes. The equation of state also includes the bulk modulus derivative  $B'$  acting as one additional free variable. Lattice parameter  $a$  is obtainable from simple triple product relation ( $V_0 = |(\vec{a} \times \vec{a}) \cdot \vec{a}|$ ). The cohesive energy by definition is

$$E_{coh} = EV_0 - n_{Si}E_{Si} + n_C E_C \quad (3.2)$$

with the total energy  $E(V_0)$  obtained in the Vinet fit, of the  $\beta$ -SiC unit cell consisting  $n_X$  of  $X$  species each, relative to their energies  $E_X$  at vacuum. The Vinet equation of state was selected over other fit as it is more robust even at increased volume spacing. This sparse data points allow us to work with less tight DMC variance, reducing the sampling length required. PZ and PBE was considered for the optimization, as they have a tendency to under and over-expand, respectively.

Table 3.1 summarizes the calculated structural properties of  $\beta$ -SiC. DMC was found to better match experimental values at the tested quantities, including only 0.9% deviation from the experimental bulk modulus, as well more accurate lattice parameter to within  $10^{-2}$  Å. In terms of cohesive energy, PBE prediction is comparable to the DMC, and somewhat higher than the experimental values. The structural optimization from PBE and PZ is inline with their well-known tendencies to over- and under-estimate lattice parameters, respectively, with DMC in the middle. Both are still reasonably accurate to within  $< 0.03$  Å of the experimental lattice. The planar and nanotube SiC has a different  $sp^2$  configuration over the  $sp^3$  of the bulk form, but they are also covalent and well studied [57, 58], thus are unexpected to present significant difficulty for the accurate structural optimization. Unless there are significant discrepancies between PZ and PBE in the later planar and nanotube SiC, it is safe to conclude that full DMC optimization is unnecessary for the base geometry of the adsorbent itself. In addition,

there have not been any successful implementation of force estimator within DMC framework, without which optimization with high degree of freedom is expensive. It appears promising, if not unexpected, however, that DMC has managed to noticeably improve upon conventional methods even for such a basic system.

Table 3.1: Calculated lattice parameter ( $a$ ), bulk modulus ( $B$ ), and cohesive energy ( $E_{\text{coh}}$ ) of  $\beta$ -SiC.

Property	LDA [68]	GGA (PBE)	DMC	Exp. [69]
$a$ (Å)	4.323	4.381	4.355	4.3596
$B$ (GPa)	250	211	227	225
$E_{\text{coh}}$ (eV/f.u.)	—	12.92	12.91(15)	12.68

### 3.1.3 Structural optimization of SiCNT

In existing literatures, periodic model is clearly preferred for modelling  $\beta$ -SiC, both cluster and periodic approximation were employed for modelling the SiCNTs [6–8, 26, 61, 70]. The two approaches differ in the simulated length of the SiCNT and their consequences. Periodic approximation models infinite length SiCNT, introducing artificial periodicity which effect has to be removed by adding vacuums within the simulation cell. On the other hand, cluster approximation model the nanotube in some finite length, including their ends, which needs to be passivated to prevent dangling bonds. In practice, the choice between periodic or cluster model is influenced by the preferred implementation of DFT code and the actual physics of the system. With most SiCNT synthesized so far in nanometer size, [11, 18, 51, 52], the periodic model is expected to be more representative of the actual SiCNT given the currently available information. Periodic model also has a benefit of being more symmetric, reducing the number of atom within the simulation cell (Figure 3.2). In cluster model, bonds near to the nanotube ends are often distorted, resulting in a more complex geometry [58].

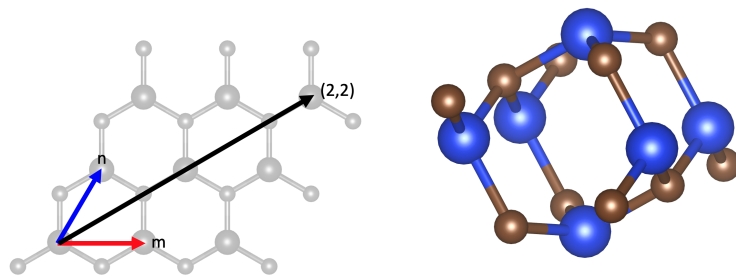


Figure 3.3: Chiral vector for classifying different SiCNT models. The end of this vector are rolled and joined together, forming the circumference of the nanotube. For example, the black arrow is the circumference for a (2,2) armchair SiCNT, with the resulting (2,2) SiCNT on the right.

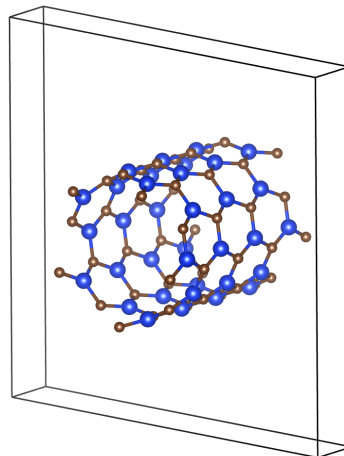


Figure 3.2: Unit cell for periodic model of an armchair (5,5) SiCNT. Solid lines mark the unit cell boundaries. The displayed atoms extend beyond the unit cell, in order to clearly show the nanotube shape.

The different sizes and configuration of SiCNTs are labelled by a quantity often referred to as “chirality”, which is a pair of integers  $(m, n)$  corresponding to the multiple of unit translations which to be folded (Figure 3.3). Armchair nanotubes corresponds to  $(n, n)$  chiralities, while zigzag corresponds to  $(n, 0)$  chiralities for some  $n$ . When the chirality is  $(m, n)$  where  $m \neq n$ , the nanotubes are referred to as just “chiral”. To see which chirality is preferred, a set of calculations with varying SiCNT size

was performed. In general, PBE and PZ reaches the same conclusion: armchair is more stable than zigzag (higher cohesive energy), especially at smaller diameter. The cohesive energies are plotted on Figure 3.4. Line plots are least-square fitting to the energies using:

$$f(d) = \frac{a}{d^2} + E_{\infty} \quad (3.3)$$

with  $a$  and  $E_{\infty}$  being the free variables, against some  $d$  diameter of the NT. This way, the asymptotic behavior of the cohesive energy as the SiCNT diameter approaches infinity (energy approaching  $E_{\infty}$ ) can be understood. Parameter  $a$  controls the line curvature but otherwise has no physical meaning. The function was found to be well fit, with the calculated  $R^2$  values for all above 0.99. The final coefficients are as follows: 1) PBE-armchair ( $-12.5773, 11.9148$ ), zigzag ( $-17.4986, 11.9816$ ); and 2) PZ-armchair ( $-12.1016, 13.1318$ ), zigzag ( $-17.0930, 13.2000$ ). From the figures and fitted coefficients, it can be understood that the cohesive energy decreases rapidly for smaller zigzag SiCNTs, thus making the armchair more energetically favorable. The crossing point is at around  $8.5 \text{ \AA}$ . At large sizes, both are almost equally stable. While there are no strong tendencies either way, given its slight edge, use, and potentially higher adsorption in existing literatures [6, 7, 61], the adsorption works on the next sections utilizes the armchair (5,5) SiCNT.

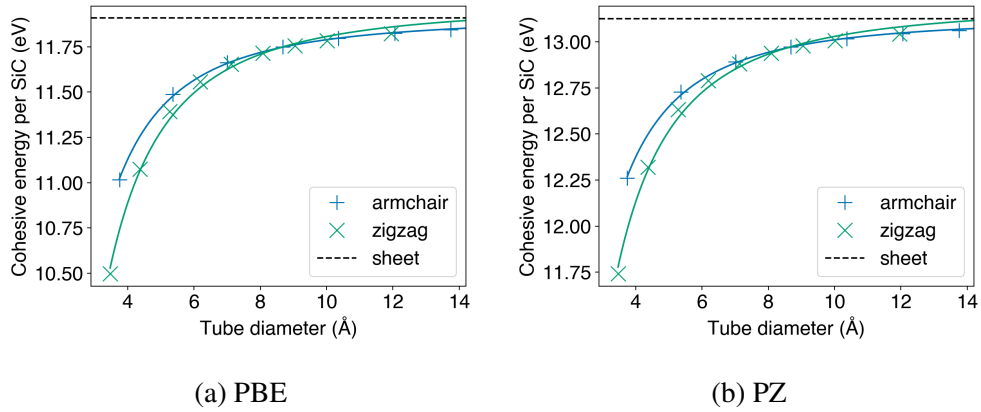


Figure 3.4: Cohesive energy vs. SiCNT diameter of armchair and zigzag SiCNT for PBE (3.4a) and PZ (3.4b) calculations. Solid lines are fitted curves in the form of Equation 3.3. The cohesive energy approaches that of sheet SiC (dashed lines) as the diameter increases. In general, armchair SiCNT has higher cohesive energy (more stable), but they are almost equal for larger diameters.

A second correlation was found between the amount of buckling and the cohesive energy (Figure 3.5). Using a slightly different fitting equation (inverse behavior w.r.t.  $d$ ):

$$f(d) = ad^2 + E_\infty \quad (3.4)$$

a good fit was achieved indicated by  $R^2$  value of more than 0.99. An outlier was found within the zigzag SiCNT, occurring at the smallest (3,0) SiCNT with the radius of just 1.73 Å. This radius is less than the Si-C bond lengths, partially explaining the unusually large distortion. With both correlates to the cohesive energy but with inverse relation, buckling radius and SiCNT diameter are inversely proportional to each other. In general, the cohesive energy of SiCNT appeared to be related to the total strain coming from both the curvature and buckling.

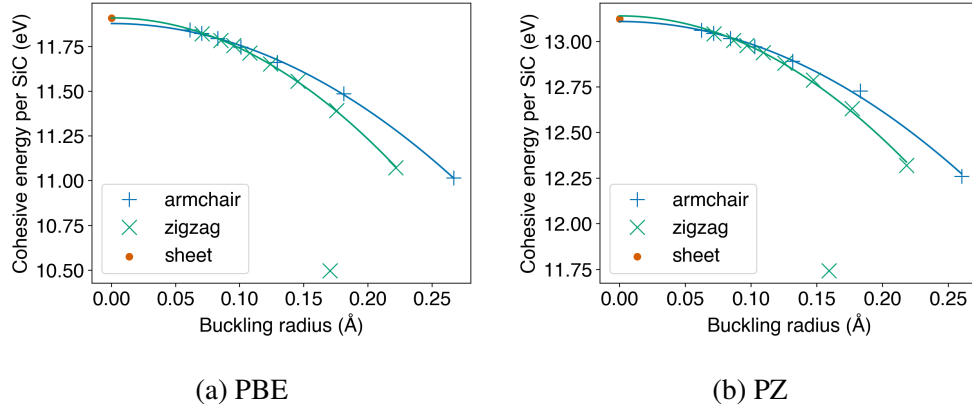


Figure 3.5: Cohesive energy vs. buckling radius for armchair and zigzag SiCNT for PBE (3.4a) and PZ (3.4b) calculations. The outlier is for (3,0) armchair where its shape is highly distorted.

Structurally, there are no significant difference whether by using PBE or PZ to optimize them. Table 3.2 (PBE) and Table 3.3 (PZ) summarizes the results. The maximum radius difference between the two methods is 0.0056 Å for (8,8) SiCNT. This difference seems to accumulate from the difference in Si-C bonds length, with them diverging with larger NTs as they contain more Si-C bonds in the circumference. The bond lengths for larger NTs approaches that of the planar SiC with 1.7880 Å and 1.7895 Å for PBE and PZ, respectively. Smaller NTs deviate larger from these values, and they buckle more. For both armchair and zigzag, the Si-C bond lengths

including the curvature are slightly longer than those parallel to the NT axis. The difference is, however, generally less than 0.01 Å. This trend were also observed by prior LDA [66, 71] and hybrid functional [57, 58, 65] works.

Table 3.2: Optimized geometries of SiCNTs using PBE exchange-correlation functional.  $d$  subscript indicates Si-C bonds with some component in the SiCNT curvature.

(n, m)	$R_{H_2}$ [Å]	$\beta$ [Å]	$\langle Si-C \rangle$ [Å]	$\langle Si-C_p \rangle$ [Å]	$\langle Si-C_d \rangle$ [Å]
<b>Armchair</b>					
(2,2)	1.8760	0.2669	1.8117	1.8140	1.8093
(3,3)	2.6789	0.1809	1.7951	1.7915	1.7987
(4,4)	3.5024	0.1293	1.7914	1.7886	1.7941
(5,5)	4.3377	0.1007	1.7900	1.7880	1.7920
(6,6)	5.1794	0.0827	1.7893	1.7878	1.7908
(7,7)	6.0243	0.0701	1.7889	1.7877	1.7901
(8,8)	6.8718	0.0610	1.7887	1.7878	1.7897
<b>Zigzag</b>					
(3,0)	1.7351	0.1704	1.8253	1.8070	1.8435
(4,0)	2.1837	0.2216	1.8069	1.7935	1.8204
(5,0)	2.6345	0.1757	1.7962	1.7872	1.8052
(6,0)	3.0920	0.1454	1.7932	1.7880	1.7985
(7,0)	3.5620	0.1240	1.7917	1.7882	1.7951
(8,0)	4.0389	0.1078	1.7908	1.7884	1.7932
(9,0)	4.5196	0.0952	1.7902	1.7884	1.7919
(10,0)	5.0035	0.0853	1.7898	1.7885	1.7911
(12,0)	5.9756	0.0706	1.7893	1.7886	1.7890

Table 3.3: Optimized geometries of SiCNTs using PZ exchange-correlation functional.  $d$  subscript indicates Si-C bonds with some component in the SiCNT curvature.

(n, m)	$R_{H_2}$ [Å]	$\beta$ [Å]	$\langle Si-C \rangle$ [Å]	$\langle Si-C_p \rangle$ [Å]	$\langle Si-C_d \rangle$ [Å]
<b>Armchair</b>					
(2,2)	1.8731	0.2601	1.8125	1.8148	1.8102
(3,3)	2.6799	0.1830	1.7963	1.7928	1.7998
(4,4)	3.5049	0.1316	1.7927	1.7900	1.7954

(5,5)	4.3414	0.1026	1.7914	1.7895	1.7934
(6,6)	5.1837	0.0842	1.7908	1.7893	1.7922
(7,7)	6.0294	0.0715	1.7904	1.7893	1.7915
(8,8)	6.8774	0.0622	1.7902	1.7893	1.7911
<b>Zigzag</b>					
(3,0)	1.7333	0.1593	1.8254	1.8080	1.8428
(4,0)	2.1844	0.2181	1.8062	1.7949	1.8174
(5,0)	2.6370	0.1769	1.7975	1.7890	1.8059
(6,0)	3.0949	0.1474	1.7946	1.7897	1.7995
(7,0)	3.5653	0.1258	1.7931	1.7899	1.7963
(8,0)	4.0424	0.1093	1.7922	1.7900	1.7944
(9,0)	4.5240	0.0967	1.7916	1.7900	1.7933
(10,0)	5.0078	0.0867	1.7912	1.7901	1.7924
(12,0)	5.9809	0.0718	1.7907	1.7901	1.7913

---

### 3.1.4 Structural optimization of H<sub>2</sub> on SiCNT

The non-chemical nature of the adsorption means that any area on the nanotube surface can be a potential host for adsorption. It is common practice to divide the surface into sites, using such terminologies as top, hollow, and bind. These names are derived from the closest item on the surface on which the hydrogen is attached to: top refers to area immediately above of some surface atom, bond to nearby of some chemical bonds, and hollow to an empty region surrounded by other atoms. All of these sites are listed on Figure 3.6. Both outer and inner surface of the nanotube are able bind the hydrogen, however the outer surface bind it more strongly [61].

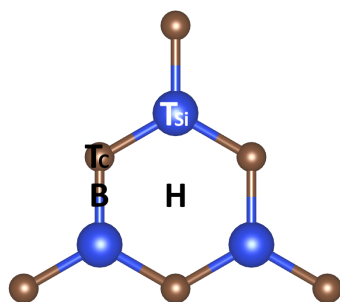


Figure 3.6: Possible hydrogen binding sites on the SiCNT surface. T = top, H = hollow, and B = bind, respectively.

To find whether any sites are preferred for the adsorption, a set of DFT optimizations were performed. Due to its buckling, silicon and carbon atom resides at slightly different distance from the nanotube center, forming two shells that both can be referred to as its surface. To ensure consistency, all reported surface-to-H<sub>2</sub> distances are defined from the outermost radius. Furthermore, the hydrogen conformation was defined in three parameters, the surface-to-H<sub>2</sub> distance ( $R_{H_2}$ ), surface angle ( $\theta_s$ ), and rotational angle ( $\theta_r$ ), as defined on Figure 3.7.

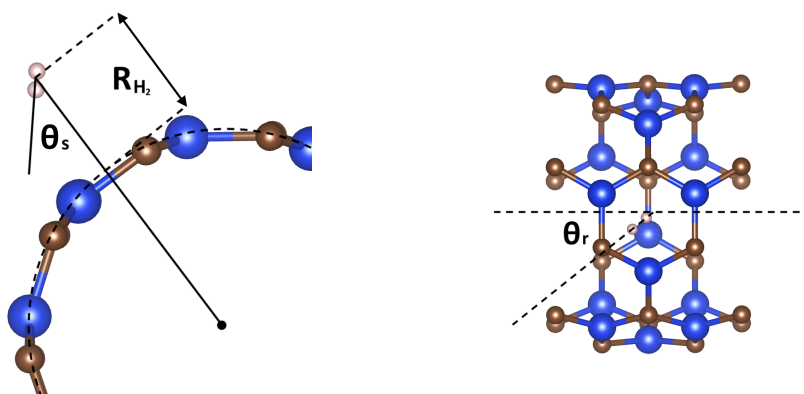


Figure 3.7: Parameters used to describe the H<sub>2</sub> conformation on the SiCNT surface. The center black dot is the nanotube axis projected perpendicularly to the paper plane. Surface angle ( $\theta_s$ ) is defined as the angle between the hydrogen's dipole axis and the normal of the tangent surface on the SiCNT nearest to the hydrogen. Rotational angle ( $\theta_r$ ) is defined as the angle between the same dipole axis and the center axis of the nanotube. Position of the hydrogen is always referenced from its geometrical center.



Adsorption energies and the previously defined conformational parameters from DFT optimization is listed on Table 3.4. Initial distances to the SiCNT surface were set at 3 Å. Consistent with the expected behavior from PZ and PBE, PZ-predicted optimized hydrogen distance is much less compared to PBE, averaging around 1 Å closer to the surface compared to the same optimization performed in PBE 3.4. The predicted binding energies are also much larger, at up to 9 times higher than PBE. This result further enforce prior observations that PZ and PBE tends to over- and under-bind on vdW-dominant systems [72, 73]. There were no appreciable change to the bond lengths compared to the isolated fragments both on the SiCNT and the hydrogen molecule, meaning that there were no significant reconfiguration of the electronic structure within those fragments.

Interestingly, ( $\theta_r$ ) tends to be constant throughout the optimization if started at 0° or 90°, resulting in two stable configurations. When started from an oblique angle, however, the initial 60° or 30°  $\theta_r$  were found to be suboptimal, instead converging to some intermediate angle depending on the site. For the surface angle ( $\theta_r$ ), its initial value was found to have little influence on the final conformation, with structures starting from different ( $\theta_s$ ) but the same ( $\theta_r$ ) ends up converging. The final angle seems to be influenced by the fact that silicon has larger atomic radius than carbon. This convergence is less tight when using PBE, but the energetic differences are still below 0.01 kcal/mol or less than 0.01 % of the adsorption energy. It is possible that this variation was caused by the optimization tolerance, and both conformation was in fact equal. In general, there are at least three stable conformations on each site, marked by their initial ( $\theta_r$ ) of 0°, 90°, and oblique. The 90° conformation are always less energetically favorable, with the hydrogen also situating at a longer distance regardless of the chosen XC. Other conformations on the other hand are almost equally stable. Carbon top ( $T^C$ ) sites are less stable than others, except when started at an oblique ( $\theta_r$ ). This, however, is caused by the optimization, as will be discussed in the next paragraph.

Table 3.4: Optimized conformation and adsorption energies of H<sub>2</sub> on the SiCNT surface. Influence from the selected exchange-correlation functional, adsorption site, and initial orientation of the hydrogen is evaluated. Letter H, B, and T refers to hollow, bottom, and top, respectively. Additional superscripts on the T sites denotes either carbon- (C) or silicon- (Si) top sites. The initial orientation is reflected by the subscripts of the “Site” column, letters (*h* and *v*) referring to the horizontal and vertical ( $\theta_s$  at 0° or 90°) angle, while the number to their initial  $\theta_r$ .

XC	Site	R <sub>H<sub>2</sub></sub> [Å]	$\theta_s$ [°]	$\theta_r$ [°]	$\langle\text{H-H}\rangle$ [Å]	$\langle\text{Si-C}\rangle$ [Å]	E <sub>ads</sub> [kcal/mol]
PBE	H <sub>v</sub>	3.437	37.6	0.0	0.7423	1.7902	0.291
	H <sub>h0</sub>	3.388	48.1	0.0	0.7423	1.7901	0.297
	H <sub>h30</sub>	3.450	55.5	46.4	0.7427	1.7902	0.360
	H <sub>h60</sub>	3.460	55.2	49.1	0.7427	1.7902	0.360
	H <sub>h90</sub>	3.522	90.0	90.0	0.7420	1.7902	0.143
PBE	B <sub>v</sub>	3.499	35.8	0.0	0.7425	1.7902	0.307
	B <sub>h0</sub>	3.472	42.8	0.0	0.7425	1.7902	0.307
	B <sub>h45</sub>	3.599	55.3	45.9	0.7426	1.7901	0.337
	B <sub>h90</sub>	3.611	90.0	90.0	0.7420	1.7902	0.182
PBE	T <sub>v</sub> <sup>Si</sup>	3.421	53.4	0.0	0.7425	1.7902	0.309
	T <sub>h0</sub> <sup>Si</sup>	3.399	59.4	0.0	0.7424	1.7901	0.307
	T <sub>h60</sub> <sup>Si</sup>	3.484	78.5	40.6	0.7427	1.7901	0.351
	T <sub>h90</sub> <sup>Si</sup>	3.620	90.0	90.0	0.7420	1.7901	0.182
PBE	T <sub>v</sub> <sup>C</sup>	3.624	3.1	0.0	0.7426	1.7901	0.284
	T <sub>h0</sub> <sup>C</sup>	3.686	10.0	0.0	0.7424	1.7902	0.284
	T <sub>h60</sub> <sup>C</sup>	3.672	37.5	83.9	0.7428	1.7901	0.341
	T <sub>h90</sub> <sup>C</sup>	4.224	90.0	90.0	0.7418	1.7902	0.092
PZ	H <sub>v</sub>	2.573	51.3	0.0	0.7631	1.7915	2.375
	H <sub>h0</sub>	2.566	52.7	0.0	0.7632	1.7915	2.375
	H <sub>h30</sub>	2.564	56.2	43.3	0.7644	1.7915	2.463
	H <sub>h60</sub>	2.565	56.1	42.8	0.7644	1.7915	2.463
	H <sub>h90</sub>	2.585	90.0	90.0	0.7634	1.7915	2.168
PZ	B <sub>v</sub>	2.560	76.8	0.0	0.7653	1.7915	2.530
	B <sub>h0</sub>	2.563	78.6	0.0	0.7653	1.7915	2.532
	B <sub>h45</sub>	2.569	80.1	12.8	0.7653	1.7915	2.534
	B <sub>h90</sub>	2.661	90.0	90.0	0.7642	1.7915	2.269
PZ	T <sub>v</sub> <sup>Si</sup>	2.570	78.1	0.0	0.7652	1.7915	2.530

	$T_{h0}^{Si}$	2.570	78.1	0.0	0.7652	1.7915	2.532
	$T_{h60}^{Si}$	2.591	85.9	32.2	0.7653	1.7915	2.539
	$T_{h90}^{Si}$	2.663	90.0	90.0	0.7641	1.7915	2.269
PZ	$T_v^C$	3.076	3.4	0.0	0.7629	1.7915	1.642
	$T_{h0}^C$	3.104	7.7	0.0	0.7630	1.7915	1.644
	$T_{h60}^C$	2.587	86.7	31.9	0.7653	1.7915	2.539
	$T_{h90}^C$	3.380	90.0	90.0	0.7606	1.7915	1.017

In some cases, the optimization runs resulted in the hydrogen moving out of their initial site (Figure 3.8). As the result, some conformations become identical: ( $T_v^{Si}/T_{h0}^{Si}$ ) to ( $B_v/B_{h0}$ ),  $B_{h90}$  with  $T_{h90}^{Si}$ , and  $T_{h60}^C$  being equivalent to  $T_{h60}^{Si}$  if using PZ and to B if using PBE. The fact that starting from a different conformation allowed for stable optimization indicates that the sites themselves is still able to host the hydrogen. However, the potential energy barrier between these sites seems to be relatively low, allowing the hydrogen to move between them.

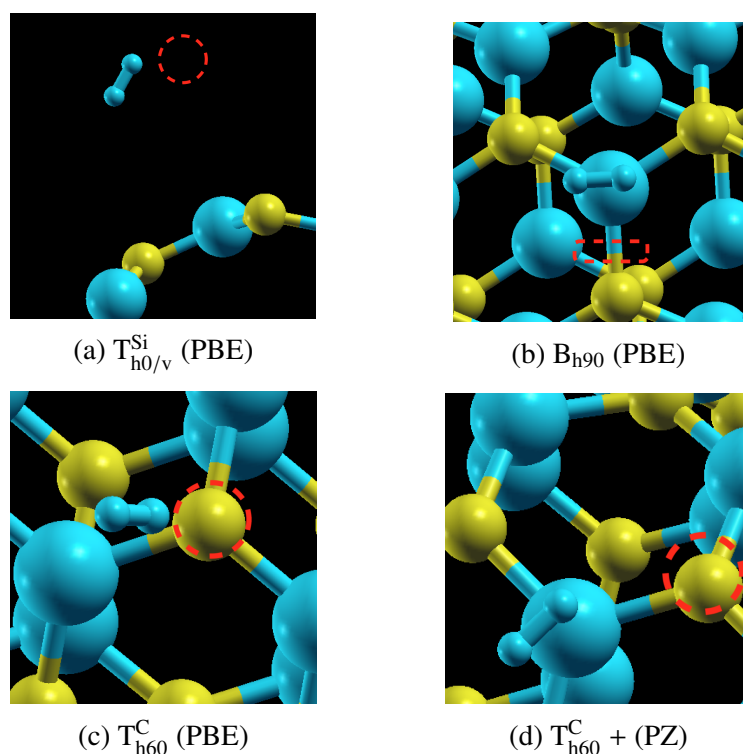


Figure 3.8: DFT optimizations where the final position of hydrogen is at a different site. Red circles indicate the initial position of the hydrogen. In (a), putting the hydrogen in vertical or horizontal position with  $0^\circ$  ( $\theta_r$ ) resulted in it being moved to an adjacent bridge site. In (b),  $B_{h90}$  is optimized to the  $T^{Si}$  site. When using PBE to optimize caused the  $T_{h60}^C$  (c) hydrogen to move to an adjacent bridge, however if PZ is instead used (d), it is moved to the nearest  $T^{Si}$ .

To inspect whether some sites are energetically preferred over another, the best cases (highest binding energy) for each site are plotted in Figure 3.9. The  $T_C$  site was found to be the least favorable for hosting the  $H_2$ , in both PBE and PZ XC, with binding energy 21% (PBE) and 32% (PZ) less relative to the most favorable site, or around 0.07 kcal/mol for PBE and 0.82 kcal/mol for PZ. One possible explanation is the SiCNT geometry: due to buckling, the carbon atoms are located further out about  $0.1 \text{ \AA}$  relative to the silicon, reducing the average interaction with another atom. The variation between the other sites are much smaller, with PBE slightly favoring hollow site, and PZ the top silicon site. Binding energies from PBE averages at  $0.348(12)$  kcal/mol when excluding  $T_C$ , while in PZ this value is at  $2.511(42)$  kcal/mol. Similarly, initial orientation of the hydrogen only minimally affects the final binding energy, except for cases where the

hydrogen is at  $90^\circ \theta_r$  (parallel to the nanotube axis). It is possible that the interaction with adjacent periodic image of the hydrogen created a local minimum high enough for the optimizer to be unable to push it out to the optimal geometry. Except for these two low energy cases, no sites are particularly preferable, thus the hollow orientation is arbitrarily chosen as the focus for the next step with DMC.

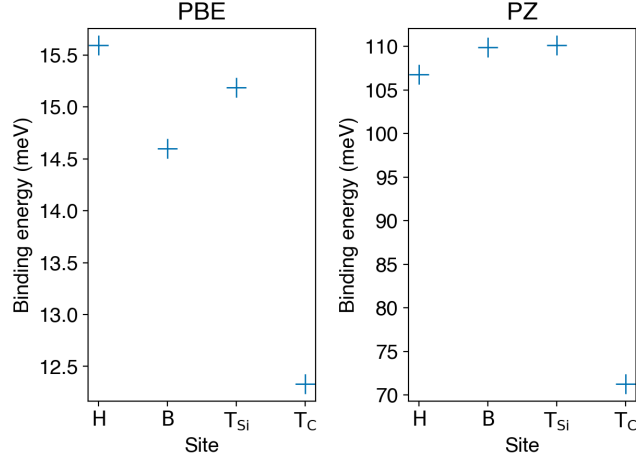


Figure 3.9: Best-case binding energy comparison between possible adsorption sites on (5,5) SiCNT. The vertical scales are adjusted for each plot due to the different magnitude between the PZ and PBE binding energies.

## 3.2 Binding energy evaluation

Binding energy is evaluated using vertical hydrogen conformation over a hollow site on the SiCNT surface, defined as:

$$E_{\text{bind}}(r) = E_{\text{SiCNT}+\text{H}_2}(r) - (E_{\text{SiCNT}} + E_{\text{H}_2}) \quad (3.5)$$

where the term inside the parenthesis are energies of separate fragments (SiCNT-only and hydrogen-only) using the same simulation cell. Here  $r$  is a scalar, since only single coordinate was varied (vertical distance over the hollow site). The binding energy is evaluated over a simulation cell consisting of 20 atoms with 80 valence electrons. The number of electrons comes from the use of pseudopotentials with He- and Ne-core for the C and Si atoms, respectively, and all electrons for the H.

Binding energy curves was obtained by fitting Morse potential over the energy values at every distance  $r$ :

$$E(r) = D_e \left( e^{-2a(r-r_e)} - 2e^{-a(r-r_e)^2} \right) + c \quad (3.6)$$

where the free variables  $D_e$ ,  $a$ , and  $r_e$  corresponds to the depth, width, and location of the minimum within the energy well, respectively. The last free variable  $c$  is not part of the typical Morse fit, and was introduced to fix size-consistency problem introduced by some of the vdW corrections, resulting in the binding energy to not converge to zero at infinity. The fitting was performed using non-linear least square Levenberg-Marquardt algorithm [74]. In DMC, each of the energy points is going to include variance. The variance is factored into the fit as an inverse weight to the residual. Then, standard error propagation can be computed from the variance over the fitting variables and plotted as a shade around the fit. The present work consider  $1\sigma$  confidence interval around the central value, which is typical for a DMC work.

### 3.3 DFT calculations

DFT calculations utilized PWSCF binary, part of the larger Quantum Espresso [75] software library. The implementation is based on plane-wave basis set and pseudopotential, modelling a system periodic by some unit cells. Burkatzki, Filippi, and Dolg [76] energy-consistent pseudopotentials were exclusively employed in all level of calculations. This pseudopotential was specifically designed to avoid singularity at the nucleus, reducing time-step error in the DMC calculation. However, it is also perfectly suitable for DFT calculation, although being a norm-conserving pseudopotential means a larger kinetic energy cut-off is required, here 150 hartree was selected. Reciprocal space integration were performed in regular Monkhorst-Pack grid [77] with  $1 \times 1 \times 6$  size. Combined, these two parameter setting achieve convergence to within 1 mHa. Structural optimization runs were performed using total force and energy thresholds of  $10^{-10}$  and  $10^{-4}$  a.u., respectively.

With the system expected to exhibit significant vdW interaction, leading vdW corrections of DFT-D2, DFT-D3, Tkatchenko-Scheffler (TS), Exchange-Dipole Model (XDM), vdW-DF2, and rVV10 was considered in this work [40, 42, 78–83]. Among

them, two groups can be discerned: asymptotic  $1/r^6$  energy correction (following vdW's long-range behavior) on the converged DFT energy, and 2<sup>nd</sup> order perturbation inclusion into the self-consistent loop. While all are somewhat calibrated with each respective vdW systems, those belonging to the second group have an additional side effect of changing the final charge density. Plain PZ [35] (LDA) and PBE [36] (GGA) calculations were also performed to provide a reference, vdW-less, DFT value.

### 3.4 VMC calculations

There are three purposes of VMC in this work: to initially check the DFT orbitals, provide energy and variance to optimize the Jastrow factors, and to prepare the set of walker configuration for the main DMC run. In all runs, a single walker is used, of which the configuration space it traces is used as a sample for either optimization or DMC. This was done to minimize the equilibration cost, as it has to be performed independently for every walker. The measure used to check the orbital quality is the ratio between the variance of local energy and its value. Without Jastrow factors added, this ratio should not exceed 0.2 Ha, whereas with Jastrow a good value is between 0.01–0.03 Ha. Should the ratio is worse than expected, DFT calculation is performed again with increased kinetic energy cut-off. The previously mentioned 150 hartree cutoff was found to be sufficient. Qualitative checks were also performed to ensure the run was stable. VMC run for optimization is 80000 steps (excluding equilibration) per optimization loop, generating those same number of samples. For DMC, the VMC was run in 4096 steps, each will become the starting point for the DMC walkers.

There are two system changes going to QMC from DFT: basis set and the boundary condition. As already explained in Chapter 2, plane-wave basis set is not computationally efficient for DMC. Starting from plane-wave orbitals as calculated by PBE-DFT, conversion to blip basis set [33] was performed using `pw2qmcpack.x` (custom patched and compiled to PWSCF). Since it is also localized, some periodic boundaries can be selectively removed, in all three-axis for the hydrogen molecule-only calculation, and in the perpendicular axes in the case of nanotube system. This has possible implication in the vacuum convergence behavior, which is to be discussed in the next chapter.

### 3.5 Trial wavefunction optimization

Optimization here refer to the parametrization of the wavefunction and the subsequent optimization of those parameters. There are many ways to do such, but in the present work this was achieved by adding a Jastrow factor to the antisymmetrized (by determinant) DFT orbitals, i.e.,

$$\Psi_T(p) = e^J(p)D_\uparrow D_\downarrow \quad (3.7)$$

with  $p$  representing the optimizable parameters, and  $D$  being the antisymmetrizing determinants. Thus, all parameters are contained within the Jastrow factor. In QMC-PACK, these factors are also in the form of B-splines. Current work employs one-body (electron-nucleus; nuclei are static), and two-body (electron-electron) Jastrow factors. Three-body (electron-electron-nucleus) Jastrow factor was not used the wavefunction quality was found to be good enough as is (by the variance / energy ratio). Each b-splines contains 10 optimizable terms. The one-body factors are different for each species (silicon, carbon, and hydrogen), while the two-body factors comes in two separate terms, of up-up and up-down interaction (referring to the two collinear spins). The factors are optimized by minimizing the VMC energy. The optimization follows hybrid scheme of Neuscamman and Otis [84], in which linear method [85] are interspersed with accelerated descent method for a faster yet tight convergence. The same Jastrow factors are shared for each respective geometry of the SiCNT and hydrogen adsorption.

### 3.6 DMC calculations

DMC is theoretically exact, however in practice several systematic biases coming from numerical approximations needs to be accounted for:

- Localization bias due to the use of nonlocal pseudopotential. Non-locality here refer to the orbital dependency of some terms within the pseudopotential itself. In some cases, DMC evaluation of nonlocal pseudopotential may cause variational principle to cease, resulting in energy bias requiring special techniques to correct. Here, the “T-move” method by Casula et al. [86, 87] was employed. The specific of the method is not the focus of this work, however it is achieved by modification to the DMC’s branching term.



- DMC timestep bias. The projector used to evolve the walker is only technically exact at 0 a.u. (no walk). Instead, a set of finite timesteps were used, from which the value at 0 a.u. is estimated from extrapolation. The present work uses 0.0025, 0.01, and 0.04 a.u. timesteps.
- Finite size error. The finite cell size introduces artificial periodicity not existing in a true infinite system. This is more severe than in DFT, as DMC is able to capture long-ranged interactions. To encounter this, the energy is extrapolated by calculating in supercells 2, 6, and 8 times duplicates in size of the primitive unit cell. With two direction as vacuum, the enlargement was done in the nanotube axis direction. Furthermore, *twists* or shifts to the boundary condition of the simulation cell was also used. The number of required twists is inverse to the size of the supercell, with each energy of the 2, 6, and 8 supercells averaged from 8, 3, and 2 twists, respectively.
- Population bias. Too small walker size is known to introduce slight shift in the DMC energy. In general, more than 1000 walkers is considered sufficient. Here 4096 walkers are set as the target, spread over 32 to 256 computational nodes.

The workflow of DMC then becomes a sequence of extrapolations, with the DMC energy obtained by first eliminating the timestep bias, followed by the finite size error elimination. In total, for every adsorption geometry, there are nine DMC runs, from three supercell sizes at three timesteps each. In addition, each of these runs are averaged from several twists, however the total number of required step is unchanged. Each run is not equal in cost, however. DMC scales at  $N^3$  with the number of electrons, thus while only consisting of a single twist, 8-supercell runs are more expensive than the smaller sizes with more twists. Furthermore, runs with larger timesteps suffer less from autocorrelation, meaning that less step is required.

# Chapter 4

## Results

### 4.1 DMC binding energy estimation

#### 4.1.1 Effect of vacuum size

Modelling non-periodic system with periodic boundary model inevitably requires enlargement of the simulation cell to exclude unwanted interactions with the periodic images. This additional size, often referred to as just the vacuum depth, is optimized by gradually increasing it until the cell's total energy converged. With DMC at its core being a many-body electron theory, it is expected to better capture weak (non-covalent) and possibly longer-ranged interactions. For that reason, converging the unit cell size in DFT does not necessarily result in an optimal unit cell size for DMC.

The convergence is shown by Figure 4.1, with the total energies of the SiCNT simulation cells plotted against the varying vacuum size. With DFT, 8 Å vacuum is sufficient to remove the unwanted interaction between one SiCNT and its periodic images. In DMC, however, this is not sufficient, with the total energy still deviates from the optimal value by  $\approx 3.5$  kcal/mol. At least 14 Å is required for convergence. Additionally, their behavior is different: in DFT the total energy increases for smaller vacuum, suggesting some kind of repulsion between the periodic SiCNT images. Since the DMC calculations were performed with some periodic boundaries removed, this kind of spurious interaction does not exist, however some deviation can still be observed due to insufficient length for the wavefunction to fully decay to vacuum, or as a result

of distortion to the node locations caused by the artificial interaction when generating them in DFT. Regardless of their physical origin, the vacuum was set to 15 Å for all DFT, VMC, and QMC to fully remove their influence to the final results.

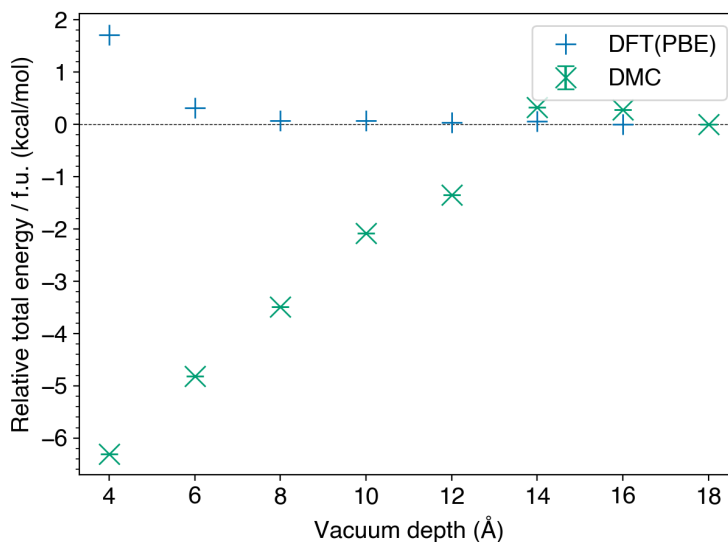


Figure 4.1: Total energy of the simulation cell relative to vacuum depth. All values are relative to the total energy at 18 Å. Green and purple points refers to the total energies from PBE-DFT and DMC calculation.

### 4.1.2 DMC binding energy

As explained in the Chapter 3, final DMC total energies is obtained after extrapolating out the timestep bias and finite size error. Note that the DMC total energies listed on Table 4.1 have varying scale of variance, this was caused by insufficient (lower than planned) runs on some systems due to computational limitation. An automated system was put in place, however, to keep the runs balanced, thus limiting the effect on the final binding energy estimation (Figure 4.2) aside from the obviously increased variance. With variance-weighted fitting performed on all extrapolation steps, the effect is further minimized. The timestep-corrected energies are listed on Table 4.2, with the final total energy of the system listed on Table 4.3.

Table 4.1: DMC total energies for every system, geometry (of adsorption), supercell, and timestep. All energies are twist-averaged, in the unit of Ha. Values in the parenthesis are  $1\sigma$  deviation from the mean value. The hydrogen calculation is not using supercell as it was performed with an open boundary condition.

System	H <sub>2</sub> distance [Å]	Supercell [times unit cell]	DMC Timestep [a.u.]	Total energy [kcal/mol]
H <sub>2</sub>	-	-	0.0025	-368.74(4)
			0.01	-368.77(3)
			0.04	-368.76(3)
SiCNT	-	2	0.0025	-3015.350(4)
			0.01	-3015.333(4)
			0.04	-3015.489(6)
		6	0.0025	-3014.669(5)
			0.01	-3014.659(4)
			0.04	-3014.826(5)
		8	0.0025	-3014.582(6)
			0.01	-3014.590(5)
			0.04	-3014.747(6)
SiCNT+H <sub>2</sub>	2.2	2	0.0025	-2774.742(6)
			0.01	-2774.729(4)
			0.04	-2774.792(4)
		6	0.0025	-2774.123(7)
			0.01	-2774.114(4)
			0.04	-2774.257(5)
		8	0.0025	-2774.058(10)
			0.01	-2774.046(5)
			0.04	-2774.198(5)
SiCNT+H <sub>2</sub>	2.43	2	0.0025	-2774.771(6)
			0.01	-2774.751(5)
			0.04	-2774.828(5)
		6	0.0025	-2774.151(7)
			0.01	-2774.148(4)
			0.04	-2774.294(4)
		8	0.0025	-2774.095(9)
			0.01	-2774.077(5)
			0.04	-2774.214(5)
			0.0025	-2774.794(4)
		2		
SiCNT+H <sub>2</sub>	2.83			

			0.01	-2774.773(4)
			0.04	-2774.861(5)
			0.0025	-2774.165(5)
		6	0.01	-2774.154(4)
			0.04	-2774.297(5)
			0.0025	-2774.091(5)
		8	0.01	-2774.094(5)
			0.04	-2774.237(5)
			0.0025	-2774.783(5)
		2	0.01	-2774.760(4)
			0.04	-2774.840(5)
			0.0025	-2774.153(7)
SiCNT+H <sub>2</sub>	3.23	6	0.01	-2774.154(4)
			0.04	-2774.297(5)
			0.0025	-2774.084(9)
		8	0.01	-2774.084(5)
			0.04	-2774.241(6)
			0.0025	-2774.772(6)
		2	0.01	-2774.765(4)
			0.04	-2774.834(5)
			0.0025	-2774.140(6)
SiCNT+H <sub>2</sub>	3.63	6	0.01	-2774.142(4)
			0.04	-2774.286(4)
			0.0025	-2774.088(8)
		8	0.01	-2774.080(5)
			0.04	-2774.217(6)
			0.0025	-2774.764(6)
		2	0.01	-2774.761(4)
			0.04	-2774.831(5)
			0.0025	-2774.127(11)
SiCNT+H <sub>2</sub>	5.0	6	0.01	-2774.125(4)
			0.04	-2774.280(5)
			0.0025	-2774.059(10)
		8	0.01	-2774.065(7)
			0.04	-2774.213(5)

Table 4.2: Timestep-extrapolated DMC total energies for every system, geometry (of adsorption), and supercell. Values in the parenthesis are  $1\sigma$  deviation from the mean value.

System	H <sub>2</sub> distance [Å]	Supercell [times unit cell]	Total energy [kcal/mol]
H <sub>2</sub>	-	-	-368.75(2)
SiCNT	-	2	-3015.319(3)
		6	-3014.637(3)
		8	-3014.554(5)
SiCNT+H <sub>2</sub>	2.2	2	-2774.723(4)
		6	-2774.085(4)
		8	-2774.009(5)
	2.43	2	-2774.746(4)
		6	-2774.115(4)
		8	-2774.051(5)
	2.83	2	-2774.772(3)
		6	-2774.131(4)
		8	-2774.068(4)
	3.23	2	-2774.758(4)
		6	-2774.120(4)
		8	-2774.044(5)
	3.63	2	-2774.755(4)
		6	-2774.107(4)
		8	-2774.051(5)
	5.0	2	-2774.748(4)
		6	-2774.082(5)
		8	-2774.029(7)

Table 4.3: Final DMC energies for every system and geometry. Values in the parenthesis are  $1\sigma$  deviation from the mean value.

System	H <sub>2</sub> distance [Å]	Total energy [kcal/mol]
--------	--------------------------------	----------------------------

H <sub>2</sub>	-	-368.75(2)
SiCNT	-	-3014.298(5)
	2.2	-2773.768(5)
	2.43	-2773.809(5)
SiCNT+H <sub>2</sub>	2.83	-2773.823(4)
	3.23	-2773.804(5)
	3.63	-2773.799(5)
	5.0	-2773.766(6)

The adsorption curve calculated from the DMC energies together with Morse fit is shown in the Figure 4.2. The curve minimum is at 1.370(107) kcal/mol, located at 2.735 Å from the SiCNT surface. This is about one third of the estimated desirable binding energy for hydrogen storage [88, 89], suggesting that pristine SiCNT may need further modification for hydrogen storage use. The value fell around the average of previous works using an assortment exchange-correlation functionals and basis sets [70, 90–92], with the only consistent trend being that this value is 0.1–0.6 kcal/mol higher than hybrid works with B3LYP, and lower by about the same range from LDA or GGA works. It is to be noted though that some of these works only evaluate the binding energy statically, without considering the full adsorption curve [70, 92], or only partially so [7], leaving the possibility for any size-inconsistency issues unchecked.

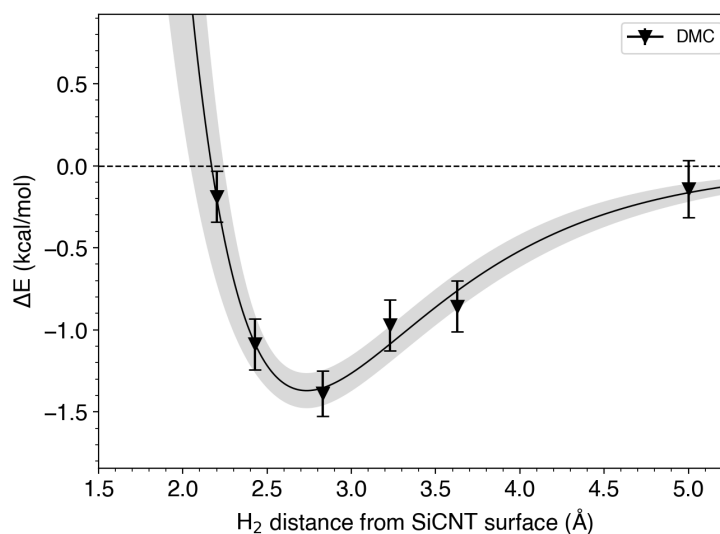


Figure 4.2: Binding energy estimation from DMC.

## 4.2 DFT binding energy estimation

Figure 4.3 shows the adsorption curve generated from conventional DFT (PBE and PZ). PZ estimates the binding energy to be 1.787 kcal/mol at 2.289 Å from the SiCNT surface, much stronger than PBE prediction at 0.2 kcal/mol at 3.198 Å. That PBE predicted weak binding is not surprising, since it does not contain the necessary nonlocal terms for describing vdW interaction, although at least one work predicted stronger binding [7], but with a different model (cluster vs. periodic here) and basis set (numerical basis set vs. plane-wave). PZ is known to have problem with self-interaction, due to its inexact exchange term. Similar observation was found on a work with atomic orbital basis set [70], with it predicting the binding energy around 1.384–2.306 kcal/mol depending on the chirality.



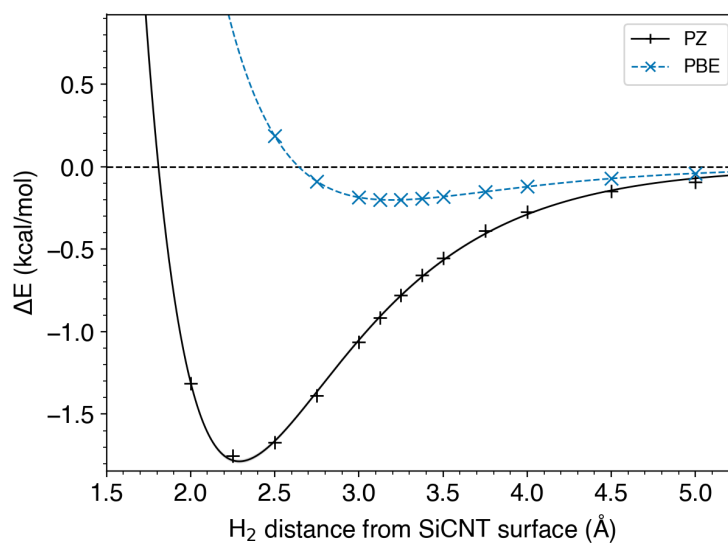


Figure 4.3: Adsorption curve from conventional DFT. PBE (GGA) predicts a much weaker interaction than PZ (LDA), almost non-binding.

Applying the pairwise correction over PBE significantly increases the predicted binding energy, into the range of between 0.904 and 1.147 kcal/mol (Figure 4.4). While all performed the correction after the SCF loop, with similar reliance on dispersion coefficients and damping terms, how the coefficients are calculated is different. DFT-D2 [37, 93] and Tkatchenko-Scheffler(TS) [40] are formally very similar, however the coefficients in TS is affected by charge density, allowing it to consider the local chemical environment. DFT-D3 [38] improves over DFT-D2 by adding  $r^8$  damping term with geometry-dependent dispersion coefficients. In the previous methods, the coefficients are empirical, however with exchange dipole model (XDM) [42], an exchange hole model is used instead to calculate these parameters. From the figure, it can be seen that DFT-D3 and TS performed similarly, while XDM energetics is closer to DFT-D2 albeit with the hydrogen 0.24 Å further away.

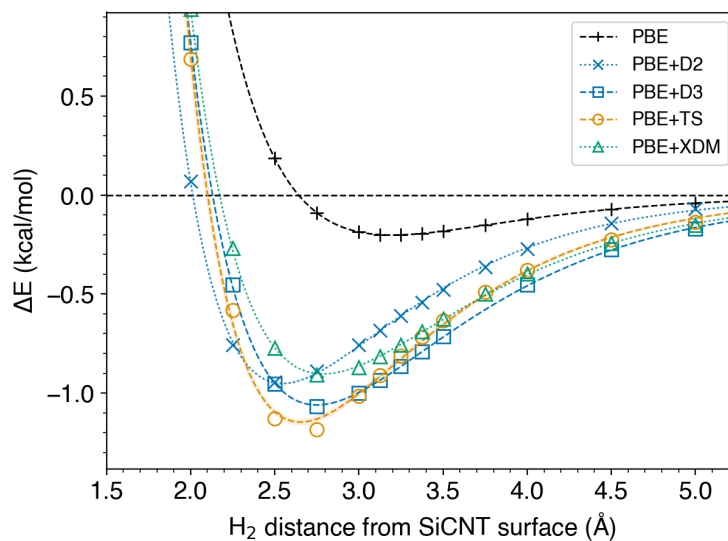


Figure 4.4: Binding energy estimation after applying pairwise correction over PBE energies. The corrections significantly strengthen the prediction, up to 1.147 kcal/mol by TS.

Comparable with the pairwise correction, the nonlocal exchange-correlations predicted the binding energy to be in the range of 1.037–1.107 kcal/mol. The vdW-DF2 puts the hydrogen 0.22 Å further away than rVV10, but are otherwise similar. Note that none of the nonlocal corrections nor the pairwise corrections predicted the binding energy at the same level as PZ, further strengthening the suspicion on spurious bonding with PZ. Further analysis to elucidate this behavior is to be discussed on the next section, which includes charge density into the picture.

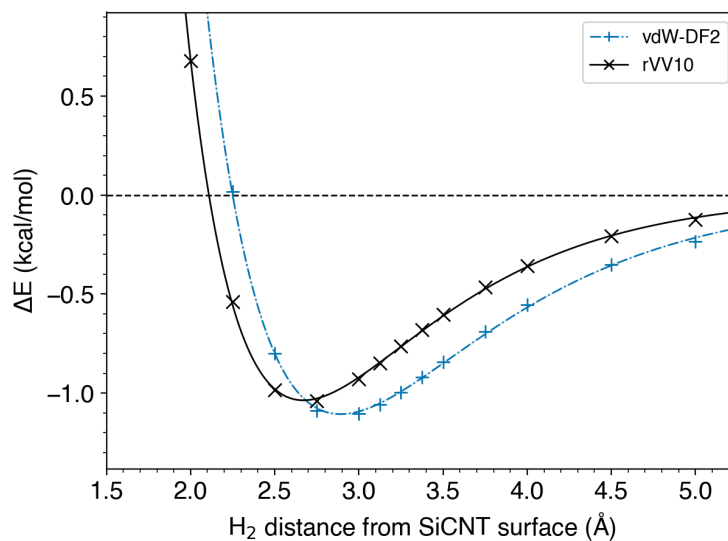


Figure 4.5: Binding energy estimation from nonlocal DFT. The predicted binding energies are qualitatively similar to that of the energy-corrected DFT.

### 4.3 Charge density analysis

Charge density is used to infer some information regarding the local chemical environment surrounding the adsorption site [73,94]. In particular, the charge density difference / redistribution, defined as

$$\Delta\rho(r) = \rho_{\text{SiCNT}+\text{H}_2}(r) - (\rho_{\text{SiCNT}}(r) + \rho_{\text{H}_2})(r) \quad (4.1)$$

is particularly useful to analyze how the charge density are changed by the interaction between the fragments, relative to their isolated behavior. The pairwise corrections (D2, D3, TS, and XDM) does not affect the charge density, thus their densities are identical to the PBE one shown in the figure. On the other hand, the non-local perturbations in the correlation integral for rVV10 and vdW-DF2 produces deformation to the charge density, as a side effect of the changes at the wavefunction level. The results for each XCs are shown in Figure 4.6.

It is immediately noticeable that vdW-DF2's charge density is unique: there is a pronounced dip in the region between the hydrogen and SiCNT surface. This indicates

no bonding is being formed, as is expected from the non-covalent nature of the vdW interaction. In contrast, the non-corrected PZ predicted charge accumulation between the  $H_2$  molecule and SiCNT, forming spurious covalent bonding. This feature is not present in the PBE data, and is instead replaced by a much weaker redistribution of charge toward the SiCNT surface. Both PZ and PBE does not treat vdW, as it does not contain nonlocal terms necessary for its description. The formation of spurious bonding in a supposedly vdW system is well known for PZ, as a result of its non-exact exchange, which in general is too weak. As a result, self-interaction (interaction of an electron with itself) is not fully cancelled out. In crystalline system, this problem often manifest itself as underestimation of the structural parameter, whereas in a molecular system, binding often formed in a region where there expected to be none. PBE is affected by this problem to some extent, although noticeably weaker. Interestingly, the rVV10 charge density is more similar to that of PZ rather than vdW-DF2. There is a precedent of this unusual behavior in a work on layered graphynes [73], where rVV10 produced inaccurate density (compared to DMC), but without seemingly affecting its energy and geometry prediction (the long range behavior was still correct).

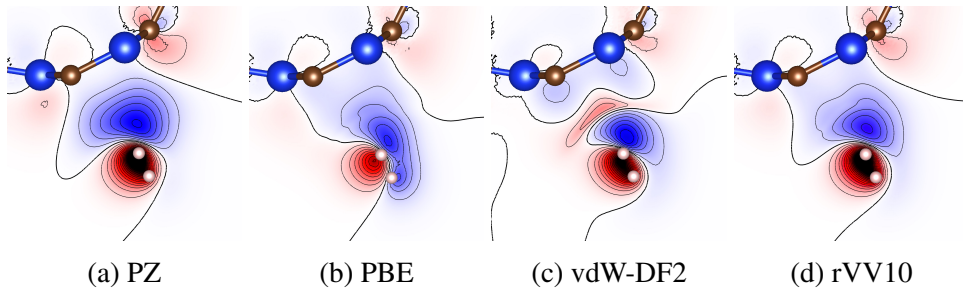


Figure 4.6: Charge density difference  $\Delta\rho(r)$  in the region near hydrogen adsorption site. The displayed plot are for each (a) PZ, (b) PBE, (c) vdW-DF2, and (d) rVV10 exchange-correlation functional. Blue and red denotes a positive/negative difference, meaning that blue region has *more* electrons that it was if the fragments are isolated.

# Chapter 5

## Discussion

### 5.1 DMC-DFT discrepancy

By design, the corrections should improve upon conventional XC when treating system with significant vdW interaction. The magnitude of this improvement, however, can be system-dependent, and may not be comprehensive: some corrections are better at energy but bad at geometry, and vice versa [73, 95]. It is not entirely unsurprising due to their nature as approximations, in contrast to a true many-body model as is the DMC. What important is to understand their behavior for each family of system, thus allowing one to decide which of the corrections is best for the given task.

The adsorption curves for each XCs and corrections relative to the DMC is shown on Figure 5.1. It is clear that PZ (PBE) severely over (under)-binds the DMC target value by 0.6 (1.2) kcal/mol. This result is consistent with the established behavior of LDA and GGA in vdW-dominated systems. The newer D3, TS, and XDM pairwise potentials better matches DMC values compared to D2, except for XDM where it is actually worse in predicting the binding energy. These newer potentials improved upon D2 by adding geometrical dependency into the dispersion coefficients. In PBE+TS, the dispersion term is dependent on local density by Hirshfeld partitioning. PBE+D3 instead inserted the dependency by coordination number, but it also added three-body term, for taking into account the effect of non-additivity, as well as adding  $r^{-8}$  term into the power expansion. XDM further expand up to  $r^{-10}$  term, and uses exchange-correlation hole model over the density to replace some of the pre-calculated coefficients, however here

it seems to only improve the geometry. Considering all started from PBE energies, this is satisfactory. The non-empirical vdW-DF2 and rVV10 nonlocal functionals return virtually identical binding energies, but their  $H_2$  separations differ by  $\sim 0.2 \text{ \AA}$ .

In general, all vdW corrections underbind relative to DMC, but the location of the minima itself is more reasonable. This suggests that while the geometries derived from these functionals can generally be trusted, energetics needs to be more carefully considered. Overall, PBE+TS produces the closest binding energy to the DMC, while the  $H_2$  distance is best reproduced by PBE+D3 (Table 5.1).

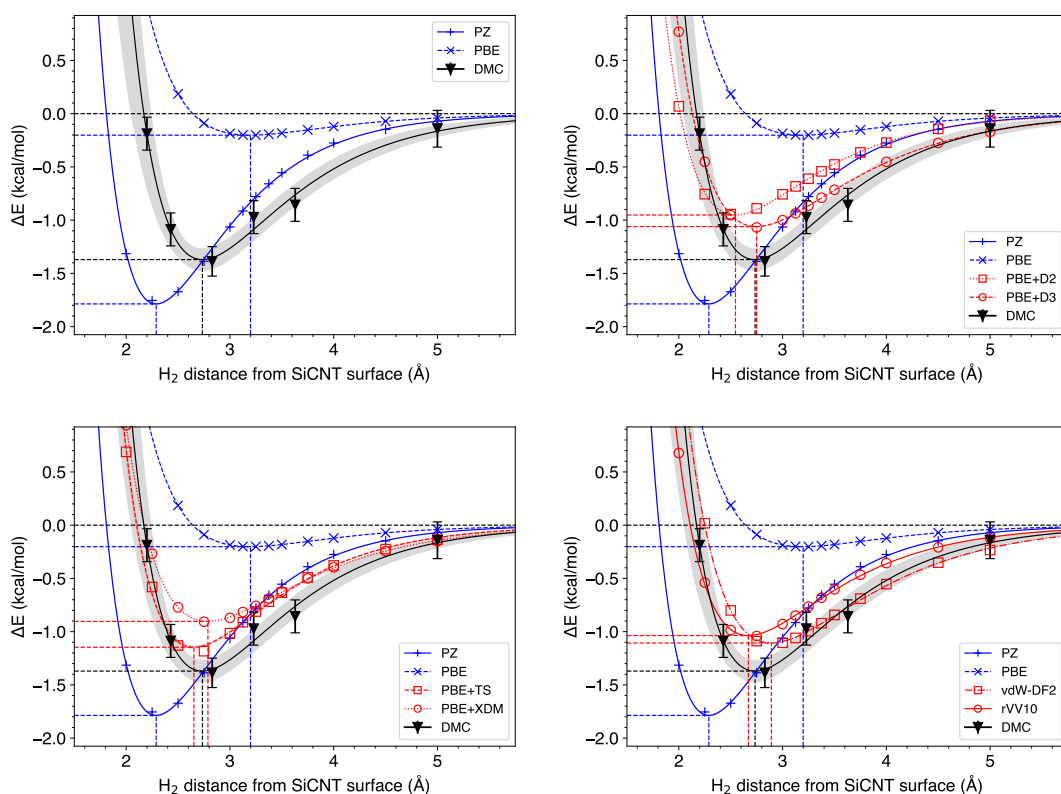


Figure 5.1: Binding energy vs.  $H_2$  distance plot for (a) conventional XCs and DMC, compared to (b) PBE + D2 and PBE + D3, (c) PBE + TS and PBE + XDM, and (d) vdW-DF2 and rVV10. Blue curves represent conventional XCs, while red and black curves represent vdW-corrected XCs and DMC, respectively. Dashed lines indicate each fitting curve's minimum. While energetically similar, the minima from the vdW-corrected XCs are at different positions, and they slightly underbind relative to DMC.

With regard to the inaccuracy of conventional XCs, LDA is known to produce spurious covalent bonding between noncovalent molecules due to the self-interaction error [95,96]. This gives rise to the ca. 0.6 kcal/mol overbinding. GGA improves the self-interaction error, but at the cost of weak intermolecular interactions as the vdW interaction is not inherently accounted for. Hence, it can be argued that the application of the corrections into GGA instead of LDA is expected to give better results, although it was not specifically examined.

Table 5.1: Binding energy estimation for vs. vertical-oriented H<sub>2</sub> distance plot from DFT of all XCs and DMC.

XC	$R_{\text{H}_2}$ [Å]	$\Delta E$ [kcal/mol]
PZ	2.289	1.787
PBE	3.198	0.202
PBE+D2	2.546	0.952
PBE+D3	2.750	1.060
PBE+TS	2.653	1.147
PBE+XDM	2.788	0.904
vdW-DF2	2.892	1.107
rVV10	2.670	1.037
DMC	2.735	1.370(106)

## 5.2 Finite size error and timestep bias

In interpreting the DMC results, it is important to discuss the extrapolations used to remove the finite size error and timestep biases. This is especially important in a non-covalent system, such as the system studied, where the magnitude of the interaction energies are relatively small. Indeed, for the SiCNT+H<sub>2</sub> complex, the absolute DMC energy between the smallest 2 unit (of the primitive cell) and the largest 8 unit supercells can differ by up to 15.82 kcal/mol, which translates to  $\sim 0.72$  kcal/mol for each atom within the unit cell, or around 52% of the target interaction energy (Figure 5.2–5.3). Despite this seemingly large size, the error was found to be reasonably well-behaved, and such was easily controlled by performing adequate statistical accumulation and the

linear extrapolation by  $1/N$  of the system size. This resulted in the final uncertainties of not more than  $\sim 0.14$  kcal/mol for each  $H_2$  distance. Due to the presence of open boundaries at the  $x$  and  $y$  plane (perpendicular to the SiCNT axis), Chiesa correction [97] could not be used to further reduce the finite size error.

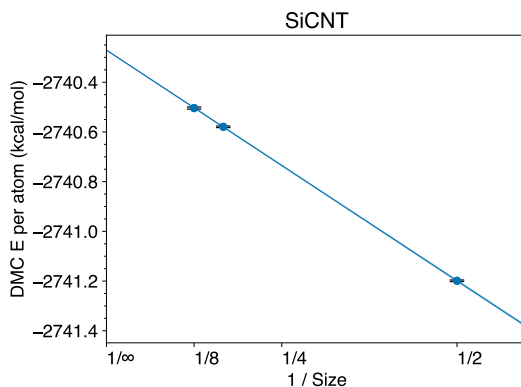


Figure 5.2: DMC finite size correction for SiCNT-only fragment.

The timestep bias on the other hand, although relatively non-linear if compared to the finite size bias, is relatively small, with the maximum of  $\sim 0.25$  kcal/mol an atom for the largest  $0.04$  a.u.<sup>-1</sup> timestep size (Figure 5.4–5.8). There is a trade-off between choosing a smaller DMC timestep and largest simulation cell and the computational cost.

### 5.3 Geometry variance with different functionals

Previously in Chapter 4 through Section 5.1, the  $H_2$  is fixed at vertical orientation with only the distance varied for the purpose of evaluating vdW interactions. Here, full geometry optimization was performed to obtain a more realistic adsorption energy. Table 5.2 summarizes the structural and energetics information from all utilized DFT methods. Similar to the previous findings in fixed vertical orientation, nonlocal vdW functionals (vdW-DF2 and rVV10) are rather similar, with LDA and GGA over and underbind, respectively, which is consistent with well-known behavior for noncovalent systems. [95] The vdW-corrected results agree well with each other, both in terms of structural parameters and adsorption energy. PBE gives relatively poor description



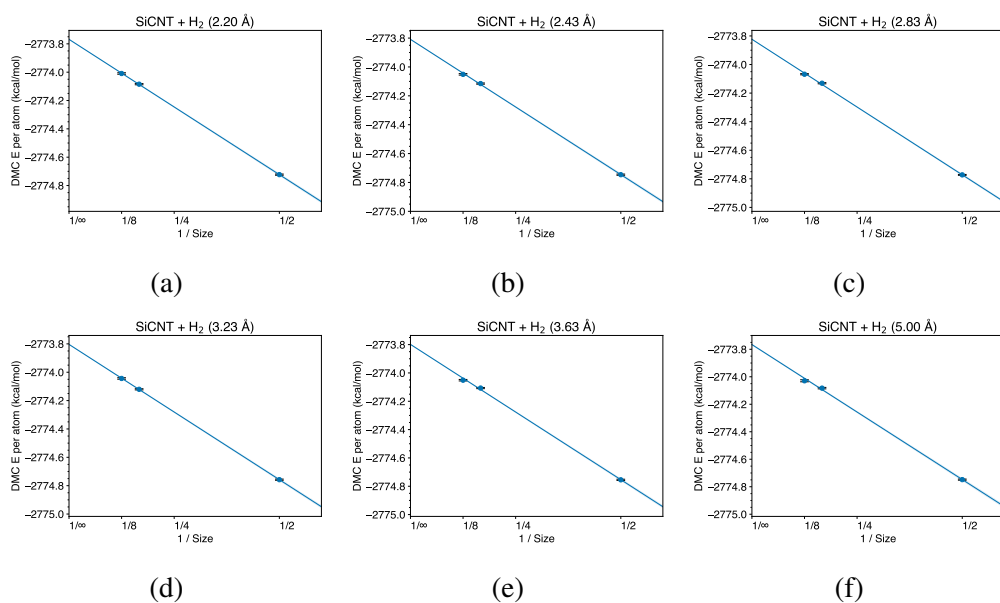


Figure 5.3: DMC finite size correction for SiCNT+H<sub>2</sub> complex, at (a) 2.20 Å, (b) 2.43 Å, (c) 2.83 Å, (d) 3.23 Å, (e) 3.63 Å, and (f) 5.00 Å distance.

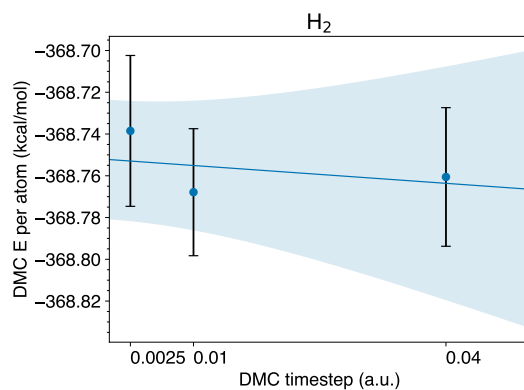


Figure 5.4: DMC timestep extrapolations for H<sub>2</sub>. Here isolated H<sub>2</sub> is used, therefore finite size extrapolation is not required.

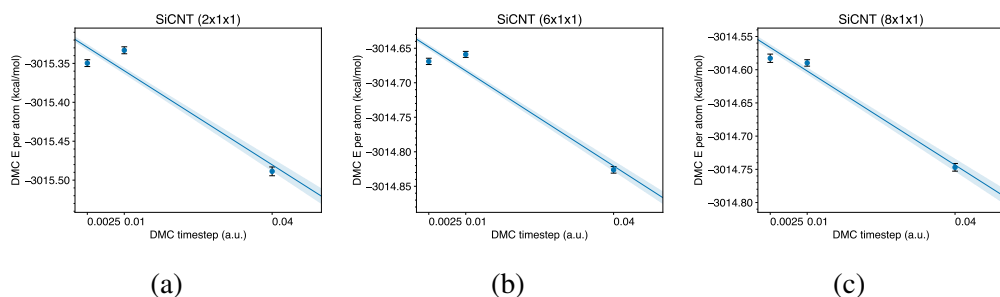


Figure 5.5: DMC timestep extrapolations for SiCNT-only fragment with (a)  $2\times 1\times 1$ , (b)  $6\times 1\times 1$ , and (c)  $8\times 1\times 1$  supercell.

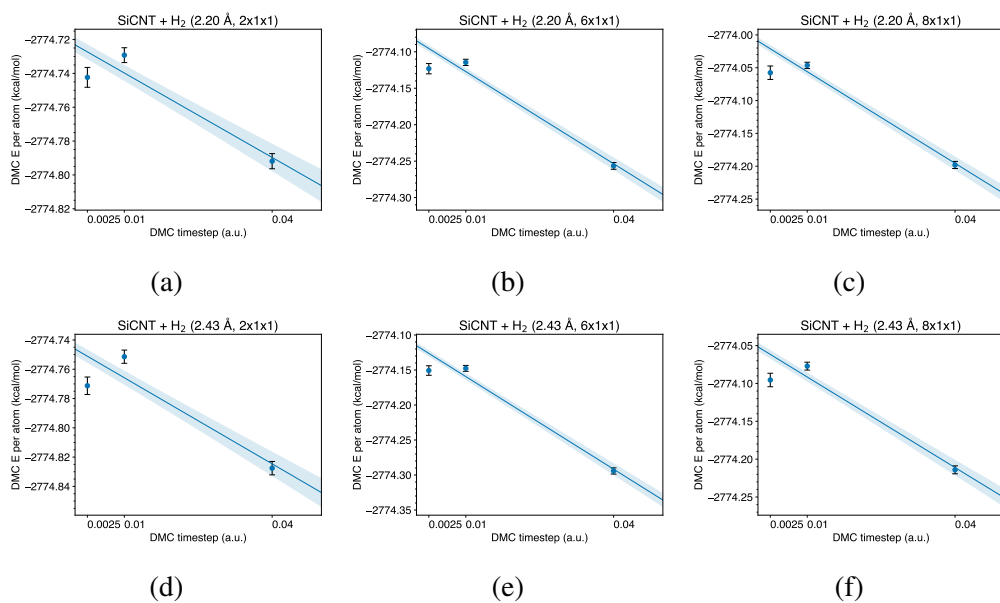


Figure 5.6: DMC timestep extrapolations for SiCNT+H<sub>2</sub> complex, at 2.20 Å distance with (a)  $2\times 1\times 1$ , (b)  $6\times 1\times 1$ , and (c)  $8\times 1\times 1$  supercell, and at 2.43 Å with (d)  $2\times 1\times 1$ , (e)  $6\times 1\times 1$ , and (f)  $8\times 1\times 1$  supercell.

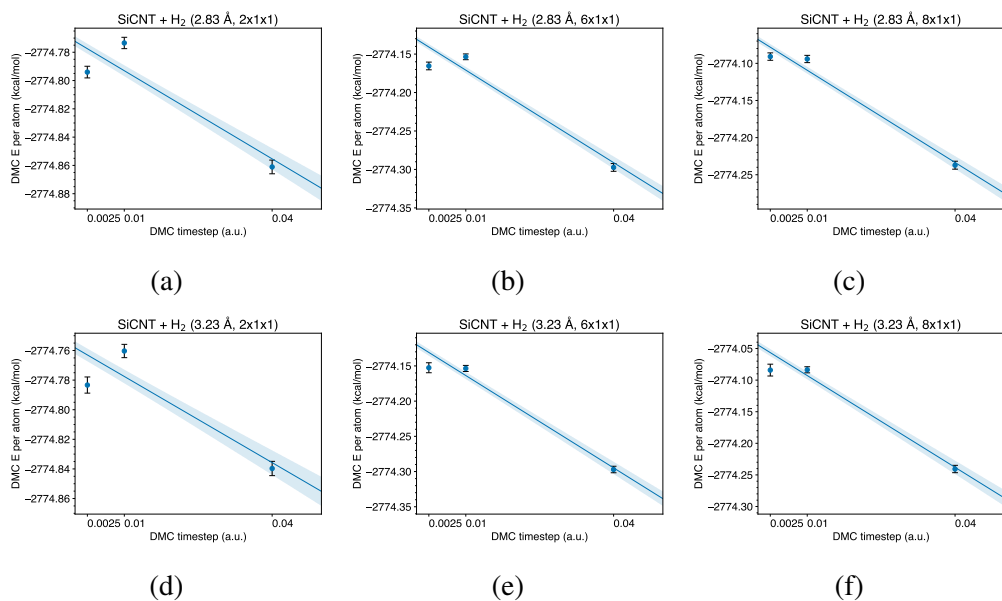


Figure 5.7: DMC timestep extrapolations for SiCNT+H<sub>2</sub> complex, at 2.83 Å distance with (a) 2×1×1, (b) 6×1×1, and (c) 8×1×1 supercell, and at 3.23 Å with (d) 2×1×1, (e) 6×1×1, and (f) 8×1×1 supercell.

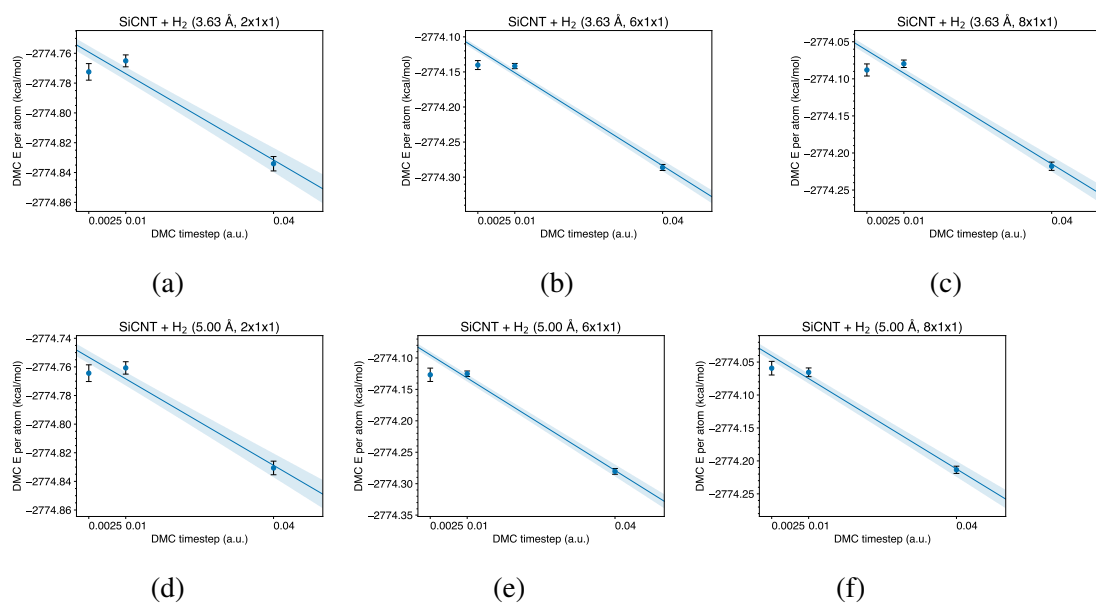


Figure 5.8: DMC timestep extrapolations for SiCNT+H<sub>2</sub> complex, at 3.63 Å distance with (a) 2×1×1, (b) 6×1×1, and (c) 8×1×1 supercell, and at 5.00 Å with (d) 2×1×1, (e) 6×1×1, and (f) 8×1×1 supercell.

compared to the vdW-corrected functionals. In contrast, LDA(PZ) still reproduces surface angle  $\theta_s$  that is closer to the nonlocal vdW corrections (vdW-DF2 and rVV10), although considering other quantities this might as well be accidental. These structural properties somewhat correlate with the charge densities previously shown in Chapter 4 (Figure 4.6). As the charge density at the (bonding) region between H<sub>2</sub> and SiCNT increases (LDA > rVV10 > vdW-DF2),  $R_{\text{H}_2}$  and  $\theta_s$  both decrease (LDA < rVV10 < vdW-DF2). As already mentioned in the previous chapter, LDA did not reproduce the noncovalent bonding, but it produced a spurious result. It is clear from the charge density and structure that the LDA overbinding correlates to the highest charge density in the bonding region.

Herein, we compare the pairwise vdW corrections to the vdW-corrected functionals. In particular, the surface angle  $\theta_s$  obtained from empirical pairwise corrections (PBE+D2/D3) is much improved over the PBE value (in a sense that they are close to the vdW-XCs), but they are still much smaller. This can be attributed to the fact that empirical corrections takes the charge densities (or wave functions through equivalence) as-is, with the total energies subtracted by the empirical pair potentials. The charge densities of the pairwise vdW corrections are the same as those of their underlying XC (PBE). In contrast, other pairwise vdW corrections (PBE+TS/XDM), while still keeping the charge density untouched, can take the local chemical environment into account. The  $\theta_s$  values is significantly improved, especially compared to the PBE value, but some underestimation remains compared to the vdW-corrected functionals. With regard to other properties, PBE+TS overestimates the adsorption energy ( $E_{\text{ads}}$ ) and underestimates the bond length ( $R_{\text{H}_2}$ ), while PBE+XDM give  $E_{\text{ads}}$  and  $R_{\text{H}_2}$  closer to the vdW functionals. Considering the above findings, it may be concluded that the self-consistent charge deformation is important, and pairwise vdW correction alone (without structural dependency elsewhere) is insufficient for accurate structure determination.

Table 5.2: H<sub>2</sub> conformations and adsorption energies from full geometry optimization.

XC	$R_{\text{H}_2}$ [Å]	$\theta_s$ [deg.]	$E_{\text{ads}}$ [kcal/mol]
PZ	2.573	51.3	2.375
PBE	3.437	37.6	0.291
PBE + D2	2.792	45.3	1.333
PBE + D3	3.000	45.7	1.421
PBE + TS	2.872	52.4	1.592
PBE + XDM	3.037	50.7	1.152
vdW-DF2	3.170	54.4	1.268
rVV10	2.930	53.9	1.298

# Chapter 6

## Summary

Adsorption properties of H<sub>2</sub> on SiCNT surface was evaluated as a representative example of molecular adsorption system used to enhance physical properties of hydrogen storages. These systems often pose a challenge to conventional *ab initio* methods, particularly DFT, due to strong influence of vdW force. This resulted in inaccurate estimation of the binding energies, structural parameters, and other related physical properties. While the origin of the biases is inherent to DFT as a single particle method, corrective schemes can and have been developed, utilizing various physics. The accuracy of the various corrections can be dependent on the target material class, necessitating external calibration. Fixed-node diffusion Monte Carlo is a compelling method to fill this role as it does not require correction for vdW, while being highly parallel, thus easily scaled given available computing power.

With regard to the adsorbent, evaluation on the stability of SiC phases, including SiCNTs at various chirality was performed. DMC was found to better predict both the bulk modulus and lattice parameters of  $\beta$ -SiC, although conventional PBE and PZ were also reasonable at less than 0.03 Å from the DMC predictions. SiC nanotubes was found to be statically stable, including the smaller sizes with less cohesive energy due to the higher distortion. The cohesive energy was found to be between 10.50–11.84 eV per f.u. when evaluated with PBE, or between 11.74–13.06 eV per f.u. evaluated with PZ, less than that of the planar and  $\beta$ -SiC. Si–C bond lengths of larger nanotubes are comparable to the planar SiC. Despite the considerable difference between PBE- and PZ-derived cohesive energies, their optimized geometries are quite similar with only up to 0.0015 Å

difference in the Si–C bond length. Armchair and zigzag chirality are almost equally stable, however there was a slight preference towards armchair type for the smaller sizes. The adsorption sites were found to be energetically similar for hosting the H<sub>2</sub>, except for the T<sub>C</sub> site, regardless of the chosen XC. Optimization with unrestricted degree of freedom on the hollow site initialized with vertical hydrogen revealed the preference for an oblique orientation, possibly due to the imbalance between the Si and C diameter.

Recently developed XC functionals designed to reproduce vdW interactions (PBE + D3, vdW-DF2, and rVV10) and conventional XC functionals (PZ, PBE) were compared to DMC as a reference. Overall, all vdW-corrected XC functionals agree well with DMC, whereas PZ (PBE) over (under)-binds. The self-consistent nonlocal correlation functionals, vdW-DF2 and rVV10, give almost the same adsorption energies. Differences in the structural properties were found to closely correlate with differences in the charge density distribution. A higher charge density in the bonding region leads to a shorter distance between H<sub>2</sub> and SiCNT and larger surface angle.

The magnitude of the vdW interaction was estimated to be ca. 1.2 kcal/mol, which corresponds to 9–29% of the ideal adsorption energy for hydrogen storage. This finding implies the importance of vdW corrections within the framework of DFT. We thus conclude that protocols based on vdW-corrected XC functionals will advance the computational investigation and exploration of storage materials in the near future. In addition, our results support previous findings that pristine SiCNT alone is unlikely to provide a sufficient binding for realizing ambient temperature hydrogen adsorption; thus, further research studies into doping and other surface modifications should be pursued to use it as the basis for a hydrogen storage system.

# References

- [1] US Department of Energy Office of Energy Efficiency and Renewable Energy. Fuel cell technologies office: Multi-year research, development, and demonstration plan, August 2015.
- [2] Ulrich Eberle, Michael Felderhoff, and Ferdi Schüth. Chemical and Physical Solutions for Hydrogen Storage. *Angew. Chem. Int. Ed.*, 48(36):6608–6630, August 2009.
- [3] C.E. Thomas. Fuel cell and battery electric vehicles compared. *Int. J. Hydrog.*, 34(15):6005–6020, August 2009.
- [4] US Department of Energy Office of Energy Efficiency and Renewable Energy. Hydrogen storage.
- [5] T. Yildirim and S. Ciraci. Titanium-Decorated Carbon Nanotubes as a Potential High-Capacity Hydrogen Storage Medium. *Phys. Rev. Lett.*, 94(17):175501, May 2005.
- [6] Chanukorn Tabtimsai, Vithaya Ruangpornvisuti, Sarawut Tontapha, and Banchob Wannoo. A DFT investigation on group 8b transition metal-doped silicon carbide nanotubes for hydrogen storage application. *Appl. Surf. Sci.*, 439:494–505, May 2018.
- [7] N. R. Devi and V. Gayathri. Effect of structural defects on the hydrogen adsorption in promising nanostructures. *Comput. Mater. Sci.*, 96:284–289, January 2015.
- [8] Giannis Mpourmpakis, George E. Froudakis, George P. Lithoxoos, and Jannis Samios. SiC Nanotubes: A Novel Material for Hydrogen Storage. *Nano Lett.*, 6(8):1581–1583, August 2006.



- [9] S. J. Mahdizadeh and E. K. Goharshadi. Hydrogen storage on silicon, carbon, and silicon carbide nanotubes: A combined quantum mechanics and grand canonical Monte Carlo simulation study. *Int. J. Hydrog.*, 39(4):1719–1731, January 2014.
- [10] Seyed Hamed Barghi, Theodore T. Tsotsis, and Muhammad Sahimi. Hydrogen sorption hysteresis and superior storage capacity of silicon-carbide nanotubes over their carbon counterparts. *Int. J. Hydrog.*, 39(36):21107–21115, December 2014.
- [11] Cuong Pham-Huu, Nicolas Keller, Gaby Ehret, and Marc J Ledoux. The First Preparation of Silicon Carbide Nanotubes by Shape Memory Synthesis and Their Catalytic Potential. *J. Catal.*, 200(2):400–410, June 2001.
- [12] M.H. Rümmeli, E. Borowiak-Palen, T. Gemming, M. Knupfer, K. Biedermann, R.J. Kalenczuk, and T. Pichler. On the formation process of silicon carbide nanophases via hydrogenated thermally induced templated synthesis. *Appl. Phys. A*, 80(8):1653–1656, May 2005.
- [13] E. Borowiak-Palen, M. H. Ruemmeli, T. Gemming, M. Knupfer, K. Biedermann, A. Leonhardt, T. Pichler, and R. J. Kalenczuk. Bulk synthesis of carbon-filled silicon carbide nanotubes with a narrow diameter distribution. *J. Appl. Phys.*, 97(5):056102, March 2005.
- [14] Nicolas Keller, Cuong Pham-Huu, Gabrielle Ehret, Valérie Keller, and Marc J. Ledoux. Synthesis and characterisation of medium surface area silicon carbide nanotubes. *Carbon*, 41(11):2131–2139, January 2003.
- [15] Tomitsugu Taguchi, Naoki Igawa, Hiroyuki Yamamoto, Shin-ichi Shamoto, and Shiro Jitsukawa. Preparation and characterization of single-phase SiC nanotubes and C-SiC coaxial nanotubes. *Phys. E: Low-Dimens. Syst. Nanostructures*, 28(4):431–438, September 2005.
- [16] T. Taguchi, N. Igawa, H. Yamamoto, and S. Jitsukawa. Synthesis of Silicon Carbide Nanotubes. *J. Am. Ceram. Soc.*, 88(2):459–461, February 2005.
- [17] Tomitsugu Taguchi, Shunya Yamamoto, Katsuaki Kodama, and Hidehito Asaoka. Synthesis of heterostructured SiC and C–SiC nanotubes by ion irradiation-induced changes in crystallinity. *Carbon*, 95:279–285, December 2015.

- [18] Xu-Hui Sun, Chi-Pui Li, Wing-Kwong Wong, Ning-Bew Wong, Chun-Sing Lee, Shuit-Tong Lee, and Boon-Keng Teo. Formation of Silicon Carbide Nanotubes and Nanowires via Reaction of Silicon (from Disproportionation of Silicon Monoxide) with Carbon Nanotubes. *J. Am. Chem. Soc.*, 124(48):14464–14471, December 2002.
- [19] Jean-Mario Nhut, Ricardo Vieira, Laurie Pesant, Jean-Philippe Tessonier, Nicolas Keller, Gaby Ehret, Cuong Pham-Huu, and Marc J Ledoux. Synthesis and catalytic uses of carbon and silicon carbide nanostructures. *Catal. Today*, 76(1):11–32, November 2002.
- [20] Yuewu Pan, Pinwen Zhu, Xin Wang, and Subei Li. Preparation and characterization of one-dimensional SiC–CNT composite nanotubes. *Diam. Relat. Mater.*, 20(3):310–313, March 2011.
- [21] Hao Wang, Xiao-Dong Li, Taek-Soo Kim, and Dong-Pyo Kim. Inorganic polymer-derived tubular SiC arrays from sacrificial alumina templates. *Appl. Phys. Lett.*, 86(17):173104, April 2005.
- [22] A. Mavrandonakis, George E. Froudakis, M. Schnell, and Max Mühlhäuser. From Pure Carbon to Silicon-Carbon Nanotubes: An Ab-initio Study. *Nano Lett.*, 3(11):1481–1484, November 2003.
- [23] Fawei Zheng, Yu Yang, and Ping Zhang. Work function of single-wall silicon carbide nanotube. *Appl. Phys. Lett.*, 97(26):263105, December 2010.
- [24] Toma Susi, Viera Skákalová, Andreas Mittelberger, Peter Kotrusz, Martin Hulman, Timothy J. Pennycook, Clemens Mangler, Jani Kotakoski, and Jannik C. Meyer. Computational insights and the observation of SiC nanograin assembly: towards 2d silicon carbide. *Sci. Rep.*, 7(1):4399, December 2017.
- [25] George E. Froudakis. Why Alkali-Metal-Doped Carbon Nanotubes Possess High Hydrogen Uptake. *Nano Lett.*, 1(10):531–533, October 2001.
- [26] Seemita Banerjee, Sandeep Nigam, C.G.S. Pillai, and Chiranjib Majumder. Hydrogen storage on ti decorated sic nanostructures: A first principles study. *Int. J. Hydrogen Energy*, 37(4):3733 – 3740, 2012.

- [27] Keishu Utimula, Rutchapon Hunkao, Masao Yano, Hiroyuki Kimoto, Kenta Hongo, Shogo Kawaguchi, Sujin Suwana, and Ryo Maezono. Machine-learning clustering technique applied to powder x-ray diffraction patterns to distinguish compositions of thmn12-type alloys. *Adv. Theory Simul.*, 3(7):2000039, 2020.
- [28] Tomohiro Yoshida, Kenta Hongo, and Ryo Maezono. First-principles study of structural transitions in linio2 and high-throughput screening for long life battery. *J. Phys. Chem. C*, 123(23):14126–14131, 2019.
- [29] Keishu Utimula, Tom Ichibha, Ryo Maezono, and Kenta Hongo. Ab initio search of polymer crystals with high thermal conductivity. *Chem. Mater.*, 31(13):4649–4656, 2019.
- [30] Anubhav Jain, Shyue Ping Ong, Geoffroy Hautier, Wei Chen, William Davidson Richards, Stephen Dacek, Shreyas Cholia, Dan Gunter, David Skinner, Gerbrand Ceder, and Kristin a. Persson. The Materials Project: A materials genome approach to accelerating materials innovation. *APL Mater.*, 1(1):011002, 2013.
- [31] Matúš Dubecký, Lubos Mitas, and Petr Jurečka. Noncovalent Interactions by Quantum Monte Carlo. *Chem. Rev.*, 116(9):5188–5215, May 2016.
- [32] M. Born and R. Oppenheimer. Zur quantentheorie der molekeln. *Ann. Phys.*, 389(20):457–484, 1927.
- [33] D. Alfé and M. J. Gillan. Efficient localized basis set for quantum Monte Carlo calculations on condensed matter. *Phys. Rev. B*, 70(16):161101, October 2004.
- [34] P. Hohenberg and W. Kohn. Inhomogeneous Electron Gas. *Phys. Rev.*, 136(3B):B864–B871, November 1964.
- [35] J. P. Perdew and Alex Zunger. Self-interaction correction to density-functional approximations for many-electron systems. *Phys. Rev. B*, 23:5048–5079, May 1981.
- [36] John P. Perdew, Kieron Burke, and Matthias Ernzerhof. Generalized gradient approximation made simple. *Phys. Rev. Lett.*, 77:3865–3868, Oct 1996.

- [37] Stefan Grimme. Semiempirical gga-type density functional constructed with a long-range dispersion correction. *J. Comput. Chem.*, 27(15):1787–1799, 2006.
- [38] Stefan Grimme, Jens Antony, Stephan Ehrlich, and Helge Krieg. A consistent and accurate ab initio parametrization of density functional dispersion correction (dft-d) for the 94 elements h-pu. *J. Chem. Phys.*, 132(15):154104, 2010.
- [39] B. M. Axilrod and E. Teller. Interaction of the van der waals type between three atoms. *J. Chem. Phys.*, 11(6):299–300, June 1943.
- [40] Alexandre Tkatchenko and Matthias Scheffler. Accurate molecular van der waals interactions from ground-state electron density and free-atom reference data. *Phys. Rev. Lett.*, 102:073005, Feb 2009.
- [41] F. L. Hirshfeld. Bonded-atom fragments for describing molecular charge densities. *Theor. Chim. Acta*, 44(2):129–138, 1977.
- [42] A. Otero-de-la Roza and Erin R. Johnson. Van der waals interactions in solids using the exchange-hole dipole moment model. *J. Chem. Phys.*, 136(17):174109, 2012.
- [43] M. Dion, H. Rydberg, E. Schröder, D. C. Langreth, and B. I. Lundqvist. Van der waals density functional for general geometries. *Phys. Rev. Lett.*, 92:246401, Jun 2004.
- [44] Kyuho Lee, Éamonn D. Murray, Lingzhu Kong, Bengt I. Lundqvist, and David C. Langreth. Higher-accuracy van der waals density functional. *Phys. Rev. B*, 82:081101, Aug 2010.
- [45] Yingkai Zhang and Weitao Yang. Comment on “generalized gradient approximation made simple”. *Phys. Rev. Lett.*, 80:890–890, Jan 1998.
- [46] John P. Perdew and Wang Yue. Accurate and simple density functional for the electronic exchange energy: Generalized gradient approximation. *Phys. Rev. B*, 33:8800–8802, Jun 1986.

- [47] Riccardo Sabatini, Tommaso Gorni, and Stefano de Gironcoli. Nonlocal van der waals density functional made simple and efficient. *Phys. Rev. B*, 87:041108, Jan 2013.
- [48] Jiyang Fan and Paul K. Chu. *Silicon Carbide Nanostructures: Fabrication, Structure, and Properties*. Springer, July 2014.
- [49] P. Mélinon, B. Masenelli, F. Tournus, and A. Perez. Playing with carbon and silicon at the nanoscale. *Nat. Mater.*, 6(7):479–490, July 2007.
- [50] Yoshiyuki Miyamoto and Byung Deok Yu. Computational designing of graphitic silicon carbide and its tubular forms. *Appl. Phys. Lett.*, 80(4):586–588, January 2002.
- [51] Zhengfang Xie, Deliang Tao, and Jiqing Wang. Synthesis of Silicon Carbide Nanotubes by Chemical Vapor Deposition. *J. Nanosci. Nanotechnol.*, 7(2):647–652, February 2007.
- [52] Andrzej Huczko, Michał Bystrzejewski, Hubert Lange, Agnieszka Fabianowska, Stanisław Cudziło, Andrzej Panas, and Mateusz Szala. Combustion Synthesis as a Novel Method for Production of 1-D SiC Nanostructures. *J. Phys. Chem. B*, 109(34):16244–16251, September 2005.
- [53] Yongfeng Zhang and Hanchen Huang. Stability of single-wall silicon carbide nanotubes – molecular dynamics simulations. *Comput. Mater. Sci.*, 43(4):664–669, October 2008.
- [54] Wang Sheng-Jie, Zhang Chun-Lai, and Wang Zhi-Guo. Melting of Single-Walled Silicon Carbide Nanotubes: Density Functional Molecular Dynamics Simulation. *Chin. Phys. Lett.*, 27(10):106101, October 2010.
- [55] Haijun Shen. MD simulations on the melting and compression of C, SiC and Si nanotubes. *J. Mater. Sci.*, 42(15):6382–6387, June 2007.
- [56] Madhu Menon, Ernst Richter, Andreas Mavrandonakis, George Froudakis, and Antonis N. Andriotis. Structure and stability of SiC nanotubes. *Phys. Rev. B*, 69(11), March 2004.

- [57] Kazi M. Alam and Asok K. Ray. Hybrid density functional study of armchair SiC nanotubes. *Phys. Rev. B*, 77(3), January 2008.
- [58] Kazi M Alam and Asok K Ray. A hybrid density functional study of zigzag SiC nanotubes. *Nanotechnology*, 18(49):495706, December 2007.
- [59] R. J. Baierle, P. Piquini, L. P. Neves, and R. H. Miwa. *Ab initio* study of native defects in SiC nanotubes. *Phys. Rev. B*, 74(15), October 2006.
- [60] Giannis Mpourmpakis, George E. Froudakis, George P. Lithoxoos, and Jannis Samios. Effect of curvature and chirality for hydrogen storage in single-walled carbon nanotubes: A Combined *ab initio* and Monte Carlo investigation. *J. Chem. Phys.*, 126(14):144704, April 2007.
- [61] Xiao Wang and K. M. Liew. Hydrogen Storage in Silicon Carbide Nanotubes by Lithium Doping. *J. Phys. Chem. C*, 115(8):3491–3496, March 2011.
- [62] Tamsyn A. Hilder, Rui Yang, Dan Gordon, Alistair P. Rendell, and Shin-Ho Chung. Silicon Carbide Nanotube as a Chloride-Selective Channel. *J. Phys. Chem. C*, 116(7):4465–4470, February 2012.
- [63] Bo Xiao, Hong Hu, Jing-xiang Zhao, and Yi-hong Ding. Functionalization of silicon carbide nanotube by dichlorocarbene: A density functional theory study. *Phys. E: Low-Dimens. Syst. Nanostructures*, 56:377–385, February 2014.
- [64] Mehdi D. Esrafil, Roghaye Nurazar, and Vahideh Masumi. Adsorption and decomposition of formamide over zigzag (n,0) silicon-carbide nanotubes (n = 5–7): Investigation of curvature effects. *Surf. Sci.*, 637-638:69–76, July 2015.
- [65] Yanli Wang, Chenhui Zhao, Kehe Su, Xin Wang, Xiulan Qin, and Zhanbing Yuan. A Density Functional Theoretical Study on Ultra Long Armchair (  $n,n$  ) Single Walled Carbon Silicon Nanotubes. *J. Nanosci. Nanotechnol.*, 17(6):3809–3815, June 2017.
- [66] Björn Baumeier, Peter Krüger, and Johannes Pollmann. Structural, elastic, and electronic properties of SiC, BN, and BeO nanotubes. *Phys. Rev. B*, 76(8), August 2007.

- [67] Pascal Vinet, John R. Smith, John Ferrante, and James H. Rose. Temperature effects on the universal equation of state of solids. *Phys. Rev. B*, 35:1945–1953, Feb 1987.
- [68] N Churcher, K Kunc, and V Heine. Calculated ground-state properties of silicon carbide. *J. Phys. C: Solid State Phys.*, 19(23):4413–4426, August 1986.
- [69] W. R. L. Lambrecht, B. Segall, M. Methfessel, and M. van Schilfgaarde. Calculated elastic constants and deformation potentials of cubic SiC. *Phys. Rev. B*, 44(8):3685–3694, August 1991.
- [70] R. J. Baierle and R. H. Miwa. Hydrogen interaction with native defects in SiC nanotubes. *Phys. Rev. B*, 76(20):205410, November 2007.
- [71] I. J. Wu and G. Y. Guo. Optical properties of SiC nanotubes: An *ab initio* study. *Phys. Rev. B*, 76(3), July 2007.
- [72] Jie Ma, Angelos Michaelides, and Dario Alfè. Binding of hydrogen on benzene, coronene, and graphene from quantum Monte Carlo calculations. *J. Chem. Phys.*, 134(13):134701, April 2011.
- [73] Hyeondeok Shin, Jeongnim Kim, Hoonkyung Lee, Olle Heinonen, Anouar Benali, and Yongkyung Kwon. Nature of Interlayer Binding and Stacking of  $sp-sp^2$  Hybridized Carbon Layers: A Quantum Monte Carlo Study. *J. Chem. Theory. Comput.*, 13(11):5639–5646, November 2017.
- [74] Jorge J. Moré. The levenberg-marquardt algorithm: Implementation and theory. In *Lecture Notes in Mathematics*, pages 105–116. Springer Berlin Heidelberg, 1978.
- [75] Paolo Giannozzi, Stefano Baroni, Nicola Bonini, Matteo Calandra, Roberto Car, Carlo Cavazzoni, Davide Ceresoli, Guido L Chiarotti, Matteo Cococcioni, Ismaila Dabo, Andrea Dal Corso, Stefano de Gironcoli, Stefano Fabris, Guido Fratesi, Ralph Gebauer, Uwe Gerstmann, Christos Gougoussis, Anton Kokalj, Michele Lazzeri, Layla Martin-Samos, Nicola Marzari, Francesco Mauri, Riccardo Mazzarello, Stefano Paolini, Alfredo Pasquarello, Lorenzo Paulatto, Carlo Sbraccia, Sandro Scandolo, Gabriele Sclausero, Ari P Seitsonen, Alexander Smogunov, Paolo Umari, and Renata M Wentzcovitch. Quantum espresso: a modular and

- open-source software project for quantum simulations of materials. *J. Phys. Condens. Matter*, 21(39):395502, 2009.
- [76] M. Burkatzki, C. Filippi, and M. Dolg. Energy-consistent pseudopotentials for quantum monte carlo calculations. *J. Chem. Phys.*, 126(23):234105, 2007.
- [77] Hendrik J. Monkhorst and James D. Pack. Special points for brillouin-zone integrations. *Phys. Rev. B*, 13:5188–5192, Jun 1976.
- [78] M. Dion, H. Rydberg, E. Schröder, D. C. Langreth, and B. I. Lundqvist. Van der waals density functional for general geometries. *Phys. Rev. Lett.*, 92:246401, Jun 2004.
- [79] Stefan Grimme. Semiempirical gga-type density functional constructed with a long-range dispersion correction. *J. Comput. Chem.*, 27(15):1787–1799, 2006.
- [80] Stefan Grimme, Jens Antony, Stephan Ehrlich, and Helge Krieg. A consistent and accurate ab initio parametrization of density functional dispersion correction (dft-d) for the 94 elements h-pu. *J. Chem. Phys.*, 132(15):154104, 2010.
- [81] Kyuho Lee, Éamonn D. Murray, Lingzhu Kong, Bengt I. Lundqvist, and David C. Langreth. Higher-accuracy van der waals density functional. *Phys. Rev. B*, 82:081101, Aug 2010.
- [82] Riccardo Sabatini, Tommaso Gorni, and Stefano de Gironcoli. Nonlocal van der waals density functional made simple and efficient. *Phys. Rev. B*, 87:041108, Jan 2013.
- [83] T. Thonhauser, S. Zuluaga, C. A. Arter, K. Berland, E. Schröder, and P. Hyldgaard. Spin signature of nonlocal correlation binding in metal-organic frameworks. *Phys. Rev. Lett.*, 115:136402, Sep 2015.
- [84] Leon Otis and Eric Neuscamman. Complementary first and second derivative methods for ansatz optimization in variational monte carlo. *Phys. Chem. Chem. Phys.*, 21:14491–14510, 2019.
- [85] Julien Toulouse and C. J. Umrigar. Optimization of quantum monte carlo wave functions by energy minimization. *J. Chem. Phys.*, 126(8):084102, 2007.



- [86] Michele Casula. Beyond the locality approximation in the standard diffusion monte carlo method. *Phys. Rev. B*, 74:161102, Oct 2006.
- [87] Michele Casula, Saverio Moroni, Sandro Sorella, and Claudia Filippi. Size-consistent variational approaches to nonlocal pseudopotentials: Standard and lattice regularized diffusion monte carlo methods revisited. *J. Chem. Phys.*, 132(15):154113, 2010.
- [88] Seung-Hoon Jhi. Activated boron nitride nanotubes: A potential material for room-temperature hydrogen storage. *Phys. Rev. B*, 74(15), October 2006.
- [89] Suresh K. Bhatia and Alan L. Myers. Optimum conditions for adsorptive storage. *Langmuir*, 22(4):1688–1700, 2006. PMID: 16460092.
- [90] Giannis Mpourmpakis, George E. Froudakis, George P. Lithoxoos, and Jannis Samios. SiC Nanotubes: A Novel Material for Hydrogen Storage. *Nano Lett.*, 6(8):1581–1583, August 2006.
- [91] N. R. Devi and V. Gayathri. Effect of structural defects on the hydrogen adsorption in promising nanostructures. *Comput. Mater. Sci.*, 96:284–289, January 2015.
- [92] Chanukorn Tabtimsai, Vithaya Ruangpornvisuti, Sarawut Tontapha, and Banchob Wannoo. A DFT investigation on group 8b transition metal-doped silicon carbide nanotubes for hydrogen storage application. *Appl. Surf. Sci.*, 439:494–505, May 2018.
- [93] Vincenzo Barone, Maurizio Casarin, Daniel Forrer, Michele Pavone, Mauro Sami, and Andrea Vittadini. Role and effective treatment of dispersive forces in materials: Polyethylene and graphite crystals as test cases. *J. Comput. Chem.*, 30(6):934–939, 2009.
- [94] Xiao Wang and K. M. Liew. Hydrogen Storage in Silicon Carbide Nanotubes by Lithium Doping. *J. Phys. Chem. C*, 115(8):3491–3496, March 2011.
- [95] Kenta Hongo, Nguyen Thanh Cuong, and Ryo Maezono. The importance of electron correlation on stacking interaction of adenine-thymine base-pair step in B-DNA: A quantum Monte Carlo study. *J. Chem. Theory Comput.*, 9(2):1081–1086, 2013.

- [96] Kenta Hongo, Mark A. Watson, Roel S. Sánchez-Carrera, Toshiaki Iitaka, and Alán Aspuru-Guzik. Failure of conventional density functionals for the prediction of molecular crystal polymorphism: A quantum monte carlo study. *J. Phys. Chem. Lett.*, 1(12):1789–1794, 2010.
- [97] Simone Chiesa, David M. Ceperley, Richard M. Martin, and Markus Holzmann. Finite-size error in many-body simulations with long-range interactions. *Phys. Rev. Lett.*, 97:076404, Aug 2006.
- [98] Koichi Momma and Fujio Izumi. *VESTA3* for three-dimensional visualization of crystal, volumetric and morphology data. *J. Appl. Crystallogr.*, 44(6):1272–1276, Dec 2011.
- [99] Genki I. Prayogo, Hyeondeok Shin, Anouar Benali, Ryo Maezono, and Kenta Hongo. Importance of van der waals interactions in hydrogen adsorption on a silicon-carbide nanotube revisited with vdw-dft and quantum monte carlo. *ACS Omega*, 6(38):24630–24636, 2021.

# List of Abbreviations

TM	Transition metal
SiC	Silicon Carbide
NT	Nanotube
SiCNT	Silicon Carbide Nanotube
f.u.	Chemical formula unit
PW	Plane wave
HF	Hartree-Fock
DFT	Density Functional Theory
LDA	Local density approximation
GGA	Generalized gradient approximation
PBE	Perdew, Burke, and Ernzerhof
PZ	Perdew-Zunger local density approximation
vdW	van der Waals
vdW-DF1	van der Waals density functional 1
vdW-DF2	van der Waals density functional 2
RVV10	Revised VV10 functional
QMC	Quantum Monte Carlo
VMC	Variational Monte Carlo
DMC	Diffusion Monte Carlo

# Biography

<b>Name</b>	Mr. Genki Imam Prayogo
<b>Date of Birth</b>	9 February 1995
<b>Educational Attainment</b>	Bachelor of Science in Engineering Physics, Bandung Institute of Technology, Bandung, Indonesia, 2016 Master of Science in Materials Science, Japan Advanced Institute of Science and Technology, Nomi, Ishikawa, Japan, 2019
<b>Scholarship</b>	2016–2019: Monbukagakusho (MEXT) Scholarship 2019–2021: JAIST Doctoral Research Fellowship (DRF) 2021–present: JAIST Jisedai Next-generation Researcher

## Publications

- [1] G. I. Prayogo, H. Shin, A. Benali, R. Maezono, K. Hongo, “SHRY: Application of Canonical Augmentation to the Atomic Substitution problem”, *J. Chem. Inf. Model.* vol. 62, pp. 2909–2915, 2022
- [2] G. I. Prayogo, H. Shin, A. Benali, R. Maezono, K. Hongo, “Importance of van der Waals Interactions in Hydrogen Adsorption on a Silicon-carbide Nanotube Revisited with vdW-DFT and Quantum Monte Carlo”, *ACS Omega*, vol. 6, pp. 24630–24636, 2021
- [3] K. Utimula, G. I. Prayogo, K. Nakano, K. Hongo, R. Maezono, “Stochastic Estimations of the Total Number of Classes for a Clustering having Extremely Large Samples to be Included in the Clustering Engine”, *Adv. Theory Simul.*, vol. 4, pp. 2000301, 2021
- [4] K. Utimula, K. Nakano, G. I. Prayogo, K. Hongo, R. Maezono, “A quantum annealing approach to ionic diffusion in solids”, *Sci. Rep.*, vol. 11, pp. 7261, 2021
- [5] T. Ichibha, G. Prayogo, K. Hongo, R. Maezono, “A new ab initio modeling scheme for ion self-diffusion coefficient applied to  $\epsilon$ -Cu<sub>3</sub>Sn phase of Cu-Sn alloy”, *Phys. Chem. Chem. Phys.*, vol. 21, pp. 5158, 2019
- [6] R. J. Hunt, M. Szyniszewski, G. I. Prayogo, R. Maezono, N. D. Drummond, “Quantum Monte Carlo calculations of energy gaps from first principles”, *Phys. Rev. B*, vol. 98, pp. 075122, 2018